View metadata, citation and similar papers at core.ac.uk

brought to you by CORE

provided by Elsevier - Publisher Connector

International Journal of Solids and Structures 49 (2012) 599–612

Contents lists available at SciVerse ScienceDirect

International Journal of Solids and Structures

journal homepage: www.elsevier.com/locate/ijsolstr

Dynamic and static asymmetric response of a layered thick disk

Michael El-Raheb

Satellite Consulting Inc., 1000 Oakforest Lane, Pasadena, CA 91107, United States

ARTICLE INFO

Article history:
Received 24 July 2011
Received in revised form 29 October 2011
Available online 13 November 2011

Keywords:
Thick layered disks
Asymmetric loading
Elasto-dynamics
Elasto-statics
Surface stresses

ABSTRACT

Treated is the asymmetric static and dynamic response of a stack of layered thick disks from external load. Variables of the three-dimensional equations are separated assuming approximate simple supports along the cylindrical perimeter, yielding non-orthogonal eigenfunctions. This also couples the truncated set of radial wave numbers. Applying a radial transform to all variables eliminates radial dependence producing a diagonal eigenproblem in all coupled axial wave numbers. Comparing 3-D and 2-D asymmetric models of industrial glass disks reveals that the 3-D resonances are close to their 2-D counterparts adopting the Mindlin model. A Fourier analysis of a specific asymmetric line-load from pressure or thermal expansion produces a scale factor to static stress from a limited number of asymmetric solutions each with a different circumferential wave number.

© 2011 Elsevier Ltd. All rights reserved.

1. Introduction

Thick disks of brittle material like glass are used as mandrills in the process of constructing accurate parabolic space antennas. Hardness and low thermal expansion are required properties when adhering the thin reflective coating to the surface of the reflector structure. These properties are met by industrial glass. Applications for space exploration require a light but stiff frame made of hot-pressed ceramics with integral ribs. Pressing the bare side of the antenna frame on the coated glass mandrill transmits asymmetric loads to the glass sometimes producing small superficial cracks near the disk center. Due to the substantial manufacturing cost of these mandrills, care is needed in the loading process to avoid damaging the surface.

Due to the circumferential and radial asymmetry in stiffness of the reflector structure, loads transmitted to the mandrill are also asymmetric. Analysis of this setup requires the solution of static and dynamic response of a thick disk forced by an asymmetric excitation. Discretization by finite elements is applicable to its solution. Yet, the asymmetry in loading requires elements throughout the mandrill volume. This translates to a large number of degrees of freedom and in turn to a substantial computational effort especially when parametric analysis is needed. Moreover, an analytical method helps comparing results with other purely numerical methods and the timely evaluation and interpretation of experimental results.

Response of thick disks is mostly treated by finite element or other purely numerical methods. Chen and Doong (1984) analyzed the vibration of initially stressed isotropic thick disks by eliminating circumferential dependence and solving the radial and axial dependence by finite difference. Chen and Chen (1988, 1989) analyzed the asymmetric buckling, vibration and dynamic stability of bi-modulus thick annular disks by a Rayleigh–Ritz finite element method. Soamidas and Ganesan (1991) analyzed the vibration of thick polar orthotropic and variable thickness disks adopting Mindlin's plate equations and a finite series expansion radially. Vinayak and Singh (1996) analyzed annular disks with holes and inclusions adopting Mindlin's equations and bi-orthogonal shape functions in a Ritz method. In all references above, normal stress is varying linearly across the thickness. Singh and Subramaniam (2003) devised a purely numerical finite element method for the vibration of thick disks and shells of revolution after eliminating the circumferential dependence. Dong (2008) analyzed the vibration of functionally graded annular disks using the Chebyshev–Ritz method. El-Raheb and Wagner (1996) analyzed the 3-D axisymmetric wave propagation in layered disks from impulsive loading. Since the present work is an extension to this analysis, a summary of the method serves as an introduction to what will follow.

Displacement vector is expressed in terms of two scalar potentials (Miklowitz, 1984) which when substituted in the Navier equations of elasto-dynamics yields two Helmholtz equations, one for each of the scalar potentials, and with wave lengths related to extensional and shear wave motions respectively. Displacements and stresses are then expressed in terms of the potentials and their derivatives. Satisfying boundary conditions on the disk cylindrical surface produces a dispersion relation in radial wave number. This process also determines axial wave number since it is related to radial wave number. Natural boundary conditions on the cylindrical surface are either traction-free where radial and shear stresses

E-mail address: mertrident@earthlink.net

0020-7683/$ - see front matter © 2011 Elsevier Ltd. All rights reserved.
doi:10.1016/j.ijsolstr.2011.11.002

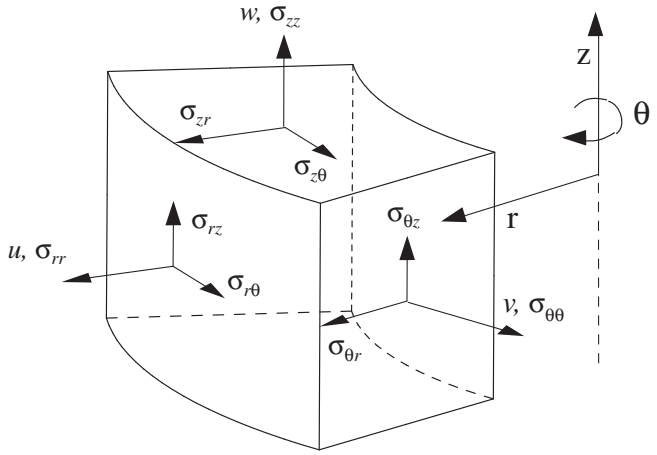

Fig. 1. Cylindrical element.

vanish, or restrained where radial and axial displacements vanish. Neither of these conditions can be satisfied exactly. An approximate alternative is to let gradient of radial displacement vanish. Although this condition is not natural to the problem, it approximates simple supports meaning that both axial displacement u and radial stress σ_{rr} on the disk perimeter (see Fig. 1) are finite but relatively small. In fact when adopting this constraint, radial wave number asymptotically approaches that of the exact simple supports at higher wave numbers. The drawback is that the problem loses its self-adjoint nature and in turn eigenfunctions become non-orthogonal.

The state vector formed of two displacements and two tractions on a layer's face is related to that on the opposite face by a transfer matrix. Continuity of state vectors at each interface of layers produces a global transfer matrix yielding an implicit eigenvalue problem. An iterative solution yields the system eigenset. Forced response follows using the static-dynamic superposition method.

Steps similar to those presented above are followed in the present analysis although the asymmetric problem is more complicated since asymmetry raises the number of independent and dependent variables. Section 2 develops the dynamic asymmetric analysis.

Section 3 develops the static asymmetric analysis. The static problem is that of the thick glass disk with one face lying on a rigid base and the other subjected to pressure applied by a stiff hexagonal lattice. A Fourier expansion of the lattice determines which circumferential wave numbers contribute to static response, namely zero and multiples of 6. Also, the expansion allows superposition of stress from the different wave number static solutions yielding an approximate estimate of maximum stress in the disk. Section 4 presents dynamic and static results.

2. Dynamic analysis

In cylindrical coordinates, the general linear elasto-dynamic equations in terms of the divergence Δ defined in (2) and rotations ψ_r, ψ_θ, ψ_z are (Love, 1944)

$$\begin{aligned}
&(\lambda+2\mu)\partial_r\Delta - 2\mu\partial_\theta\psi_z/r + 2\mu\partial_z\psi_\theta/r - \rho\partial_{tt}u = 0\\
&(\lambda+2\mu)\partial_\theta\Delta/r - 2\mu\partial_z\psi_r + 2\mu\partial_r\psi_z - \rho\partial_{tt}\upsilon = 0\\
&(\lambda+2\mu)\partial_z\Delta - 2\mu\partial_r(r\psi_\theta)/r + 2\mu\partial_\theta\psi_r/r - \rho\partial_{tt}w = 0
\end{aligned} \tag{1}$$

λ, μ are Lame' constants, (r,θ,z) are radial, circumferential and axial coordinates, (u,υ,w) are displacements along (r,θ,z) (see Fig. 1), t is time, and

$$\begin{aligned}
&\Delta = \nabla\cdot\mathbf{u} \equiv 1/r\partial_r(ru) + 1/r\partial_\theta\upsilon + \partial_z w\\
&2\psi_r = 1/r\partial_\theta w - \partial_z\upsilon, \quad 2\psi_\theta = \partial_z u - \partial_r w, \quad 2\psi_z = 1/r(\partial_\theta(r\upsilon) - \partial_\theta u)
\end{aligned} \tag{2}$$

For harmonic motions in time with radian frequency ω, assume the expansions

$$\begin{aligned}
u(r,\theta,z;t) &= \sum_n\sum_k u_{nk}(z)J_n'(\gamma_k r)\cos(n\theta)\mathrm{e}^{\hat{\imath}\omega t}\\
\upsilon(r,\theta,z;t) &= \sum_n\sum_k \upsilon_{nk}(z)J_n(\gamma_k r)\sin(n\theta)\mathrm{e}^{\hat{\imath}\omega t}\\
w(r,\theta,z;t) &= \sum_n\sum_k w_{nk}(z)J_n(\gamma_k r)\cos(n\theta)\mathrm{e}^{\hat{\imath}\omega t}
\end{aligned} \tag{3}$$

is a solution to Eq. (1), where n is an integer wave number along the circumferential coordinate θ, $J_n(\gamma_k r)$ is the Bessel function satisfying radial dependence of the governing equations, $(\,)'$ is derivative with respect to the argument, γ_k is radial wave number, and $\hat{\imath}=\sqrt{-1}$. Since the trigonometric functions in θ are exact eigenfunction satisfying circumferential dependence of the separated equations, they are dropped temporarily in the expressions for shortness. Substituting (3) in (2) then in (1) yields

$$\begin{aligned}
&\sum_k \{\mu u_{nk}''(z) + \left((\lambda+\mu)n^2/r^2 - (\lambda+2\mu)\gamma_k^2 + \rho\omega^2\right)u_{nk}(z)\\
&\quad +(\lambda+\mu)\gamma_k n\upsilon_{nk}(z)/r + (\lambda+\mu)\gamma_k w_{nk}'(z)\}J_n'(\gamma_k r)\\
&\quad -\{2(\lambda+2\mu)n^2/(\gamma_k r^3)u_{nk}(z) + (\lambda+3\mu)n\upsilon_{nk}(z)/r^2\}J_n(\gamma_k r) = 0
\end{aligned} \tag{4a}$$

$$\begin{aligned}
&\sum_k \{\mu u_{nk}''(z) + \left((\lambda+\mu)n^2/r^2 - (\lambda+2\mu)\gamma_k^2 + \rho\omega^2\right)u_{nk}(z)\\
&\quad +(\lambda+\mu)\gamma_k n\upsilon_{nk}(z)/r + (\lambda+\mu)\gamma_k w_{nk}'(z)\}J_n'(\gamma_k r)\\
&\quad -\{2(\lambda+2\mu)n^2/(\gamma_k r^3)u_{nk}(z) + (\lambda+3\mu)n\upsilon_{nk}(z)/r^2\}J_n(\gamma_k r) = 0
\end{aligned} \tag{4b}$$

$$\begin{aligned}
&\sum_k \{(\lambda+2\mu)w_{nk}''(z) - \mu\gamma_k^2 w_{nk}(z) + (\lambda+\mu)/\gamma_k\left(n^2/r^2 - \gamma_k^2\right)u_{nk}'(z)\\
&\quad +(\lambda+\mu)n\upsilon_{nk}'(z)/r + \rho\omega^2 w_{nk}(z)\}J_n(\gamma_k r) = 0
\end{aligned} \tag{4c}$$

Define the matrix coefficients

$$\begin{aligned}
a_{kk'p} &= \int_0^a J_n'(\gamma_k r)J_n'(\gamma_{k'} r)r^{(1-p)}dr,\\
b_{kk'p} &= \int_0^a J_n'(\gamma_k r)J_n(\gamma_{k'} r)r^{(1-p)}dr,\\
c_{kk'p} &= \int_0^a J_n(\gamma_k r)J_n(\gamma_{k'} r)r^{(1-p)}dr
\end{aligned} \tag{5}$$

In (5), a is disk radius. Multiplying (4a) by $rJ_n'(\gamma_j r)$, (4b) and (4c) by $rJ_n(\gamma_j r)$, then integrating from 0 to a utilizing (5) produces a set of coupled second order ordinary differential equations in $u_{n\,k}$, υ_{nk}, $w_{n\,k}$ with constant coefficients

$$\begin{aligned}
&\sum_k \Big[\Big(\left(1-k_d^2\gamma_k^2\right)a_{kj0} + \left(k_d^2-k_s^2\right)n^2 a_{kj2} + 2k_d^2 n^2 b_{jk3}/\gamma_k - k_s^2 n^2 a_{kj2}\Big)u_{nk}(z)\\
&\quad +k_s^2 a_{kj0}u_{nk}''(z) + \Big(\left(k_d^2-k_s^2\right)n\gamma_k a_{kj1} - \left(k_d^2+k_s^2\right)nb_{kj2}\Big)\upsilon_{nk}(z)\\
&\quad +\left(k_d^2-k_s^2\right)\gamma_k a_{kj0}w_{nk}'(z)\Big] = 0
\end{aligned} \tag{6a}$$

$$\begin{aligned}
&\sum_k \Big[n\Big(\left(k_d^2-k_s^2\right)\left(\gamma_k^2 c_{kj1} - n^2 c_{kj3}\right)/\gamma_k - k_s^2 nb_{kj2}\Big)u_{nk}(z) + k_s^2 c_{kj0}\upsilon_{nk}''(z)\\
&\quad -\Big(n^2\left(k_d^2-k_s^2\right)c_{jk2} + k_s^2\left(\gamma_k^2 c_{kj0} + \gamma_k b_{kj1} + c_{kj2}\right)\Big)\upsilon_{nk}(z)\\
&\quad -n\left(k_d^2-k_s^2\right)c_{kj1}w_{nk}'\Big] = 0
\end{aligned} \tag{6b}$$

$$\sum_k \Big[-\Big(k_d^2-k_s^2\Big)/\gamma_k\big(\gamma_k^2 c_{kj0}-n^2 c_{kj2}\big)u'_{nk}(z)+n\Big(k_d^2-k_s^2\Big)c_{kj1}\upsilon'_{nk}(z) +k_d^2 c_{kj0}w''_{nk}(z)+c_{kj0}\Big(1-k_s^2\gamma_k^2\Big)w_{nk}(z)\Big]=0$$
$$k_d^2=(\lambda+2\mu)/\rho\omega^2,\quad k_s^2=2\mu/\rho\omega^2 \tag{6c}$$

To convert (6) into a standard eigen-matrix, diagonalize the terms factoring u''_{nk}, υ''_{nk}, w''_{nk} by multiplying (6a) by $a_{kj0}^{-1}\equiv\bar{a}_{kj0}$, and (6b) and (6c) by $c_{kj0}^{-1}\equiv\bar{c}_{kj0}$

$$\sum_k\Big[\Big(\delta_{jk}\Big(1-k_d^2\gamma_k^2\Big)+n^2\Big(k_d^2-k_s^2\Big)e_{jk}+2k_d^2n^2o_{jk}/\gamma_k-k_s^2n^2e_{jk}\Big)u_{nk}(z) +k_s^2\delta_{jk}u''_{nk}(z)+\Big(n\Big(k_d^2-k_s^2\Big)\gamma_k d_{jk}-n\Big(k_d^2+k_s^2\Big)f_{jk}\Big)\upsilon_{nk}(z) +\Big(k_d^2-k_s^2\Big)\gamma_k\delta_{jk}w'_{nk}(z)\Big]=0 \tag{7a}$$

$$\sum_k\Big[\Big(n\Big(k_d^2-k_s^2\Big)\big(\gamma_k^2g_{jk}-n^2l_{jk}\big)/\gamma_k-k_s^2n\bar{n}_{jk}\Big)u_{nk}(z)+k_s^2\delta_{jk}\upsilon''_{nk}(z) -\Big(n^2\Big(k_d^2-k_s^2\Big)h_{jk}+k_s^2\big(\gamma_k^2\delta_{jk}+\gamma_k m_{jk}+h_{jk}\big)\Big)\upsilon_{nk}(z) -n\Big(k_d^2-k_s^2\Big)g_{jk}w'_{nk}(z)\Big]=0 \tag{7b}$$

$$\sum_k\Big[-\Big(k_d^2-k_s^2\Big)\big(\gamma_k^2\delta_{jk}-n^2h_{jk}\big)u'_{nk}(z)/\gamma_k+n\Big(k_d^2-k_s^2\Big)g_{jk}\upsilon'_{nk}(z) +k_d^2\delta_{jk}w''_{nk}(z)+\delta_{jk}\Big(1-k_s^2\gamma_k^2\Big)w_{nk}(z)\Big]=0 \tag{7c}$$

$$d_{kj}=\sum_q^N\bar{a}_{kq0}a_{qj1},\quad e_{kj}=\sum_q^N\bar{a}_{kq0}a_{qj2},\quad f_{kj}=\sum_q^N\bar{a}_{kq0}b_{qj2}$$
$$g_{kj}=\sum_p^N\bar{c}_{kq0}c_{qj1},\quad h_{kj}=\sum_q^N\bar{c}_{kq0}c_{qj2},\quad l_{kj}=\sum_q^N\bar{c}_{kq0}b_{qj3} \tag{7d}$$
$$m_{kj}=\sum_q^N\bar{c}_{kq0}b_{qj1},\quad \bar{n}_{kj}=\sum_q^N\bar{c}_{kq0}b_{qj2},\quad o_{kj}=\sum_q^N\bar{a}_{kq0}b_{qj3}$$

δ_{kj} is the Kroneker delta, and in (7d) the number of γ_k is truncated to N. Since in Eqs. (7a)–(7c) coefficients of the z-dependence are constants, these equations admit a solution in the form:

$$u_{ns}(z)=\sum_{k=1}^N u_{nks}e^{\alpha_{ns}z},\quad \upsilon_{ns}(z)=\sum_{k=1}^N\upsilon_{nks}e^{\alpha_{ns}z},\quad w_{ns}(z)=\sum_{k=1}^N w_{nks}e^{\alpha_{ns}z} \tag{8}$$

Substituting (8) in (7) yields a set of matrix equations in the $6N$ unknowns $\{\mathbf{u},\upsilon,\mathbf{w},\mathbf{u}',\upsilon',\mathbf{w}'\}_{ns}$

$$\mathbf{u}'_{ns}-\boldsymbol{\alpha}_{ns}\mathbf{u}_{ns}=0$$
$$\boldsymbol{\upsilon}'_{ns}-\boldsymbol{\alpha}_{ns}\boldsymbol{\upsilon}_{ns}=0 \tag{9a}$$
$$\mathbf{w}'_{ns}-\boldsymbol{\alpha}_{ns}\mathbf{w}_{ns}=0$$

$$\mathbf{A}^{uu}\mathbf{u}_{ns}+\mathbf{A}^{u\upsilon}\boldsymbol{\upsilon}_{ns}+\mathbf{B}^{uw}\mathbf{w}'_{ns}-\boldsymbol{\alpha}_{ns}\mathbf{u}'_{ns}=\mathbf{0}$$
$$\mathbf{A}^{\upsilon u}\mathbf{u}_{ns}+\mathbf{A}^{\upsilon\upsilon}\boldsymbol{\upsilon}_{ns}+\mathbf{B}^{\upsilon w}\mathbf{w}'_{ns}-\boldsymbol{\alpha}_{ns}\boldsymbol{\upsilon}'_{ns}=\mathbf{0} \tag{9b}$$
$$\mathbf{A}^{ww}\mathbf{w}_{ns}+\mathbf{B}^{wu}\mathbf{u}'_{ns}+\mathbf{B}^{w\upsilon}\boldsymbol{\upsilon}'_{ns}-\boldsymbol{\alpha}_{ns}\mathbf{w}'_{ns}=\mathbf{0}$$

$\mathbf{u}_{ns}=\{u_{n\ k\ s}\}^T$, $\boldsymbol{\upsilon}_{ns}=\{\upsilon_{nk\ s}\}^T$, $\mathbf{w}_{ns}=\{w_{nks}\}^T$, $\boldsymbol{\alpha}_{ns}$ is a diagonal matrix and

$$A_{jk}^{uu}=-\Big[\delta_{jk}-k_d^2\big(\gamma_k^2\delta_{jk}-n^2e_{jk}+2n^2o_{jk}/\gamma_k\big)-k_s^2n^2e_{jk}\Big]/k_s^2$$
$$A_{jk}^{u\upsilon}=-n\Big[\Big(k_d^2-k_s^2\Big)\gamma_k d_{jk}-\Big(k_d^2+k_s^2\Big)f_{jk}\Big]/k_s^2,\ A_{jk}^{ww}=-\delta_{jk}\Big(1-k_s^2\gamma_k^2\Big)/k_d^2$$
$$A_{jk}^{\upsilon u}=-n\Big[\big(\gamma_k^2g_{jk}-n^2l_{jk}\big)\Big(k_d^2-k_s^2\Big)/\gamma_k-2k_s^2\bar{n}_{kj}\Big]/k_s^2$$
$$A_{jk}^{\upsilon\upsilon}=-\Big[\delta_{jk}-k_d^2n^2h_{jk}+k_s^2\big((n^2-1)h_{jk}-\gamma_k^2\delta_{jk}\big)\Big]/k_s^2$$
$$B_{jk}^{uw}=-\Big(k_d^2-k_s^2\Big)\gamma_k\delta_{jk}/k_s^2,\ B_{jk}^{\upsilon w}=\Big(k_d^2-k_s^2\Big)ng_{jk}/k_s^2$$
$$B_{jk}^{wu}=\Big(k_d^2-k_s^2\Big)\big(\gamma_k^2\delta_{jk}-n^2h_{jk}\big)/(\gamma_k k_d^2),B_{jk}^{w\upsilon}=-\Big(k_d^2-k_s^2\Big)ng_{jk}/k_d^2 \tag{9c}$$

A condensed form of (9) follows

$$\mathbf{Y}_{ns}-\boldsymbol{\alpha}_{ns}\mathbf{X}_{ns}=\mathbf{0}$$
$$\bar{\mathbf{A}}\mathbf{X}_{ns}+\bar{\mathbf{B}}\mathbf{Y}_{ns}-\boldsymbol{\alpha}_{ns}\mathbf{Y}_{ns}=\mathbf{0} \tag{10}$$
$$\mathbf{X}_{ns}=\{\mathbf{u},\upsilon,\mathbf{w}\}_{ns}^T,\quad \mathbf{Y}_{ns}=\{\mathbf{u}',\upsilon',\mathbf{w}'\}_{ns}^T$$

$\bar{\mathbf{A}}$ and $\bar{\mathbf{B}}$ in (10) are the ensemble of all matrices in (9b). Eq. (10) is in the form of a diagonal eigen-matrix with eigenvalues α_{ns}, $s=1,6N$. To determine γ_k assume the approximate boundary condition

$$J_n''(\gamma_k a)=0 \tag{11}$$

where a is disk radius. This condition satisfies $\partial_r u(a)=0$. For each α_{ns} corresponds an eigenvector $\{\mathbf{X}_{ns},\mathbf{Y}_{ns}\}^T=\{\{\mathbf{u},\upsilon,\mathbf{w}\}_{ns},\{\mathbf{u}',\upsilon',\mathbf{w}'\}_{ns}\}^T$ within a multiplicative constant C_{nsk}.

To determine the transfer matrix relating conjoined segments, define the state vector

$$\mathbf{S}_{ns}=\{\mathbf{u},\boldsymbol{\sigma}\}_{ns}^T,\quad \mathbf{u}_{ns}=\{u,\upsilon,w\}_{ns}^T,\quad \boldsymbol{\sigma}_{ns}=\{\sigma_{zz},\sigma_{rz},\sigma_{\theta z}\}_{ns}^T \tag{12}$$

with stresses

$$\sigma_{zzns}=\sum_k^N\big[-\lambda\big(\gamma_k^2-n^2/r^2\big)u_{nsk}/\gamma_k +\lambda n\upsilon_{nsk}/r+(\lambda+2\mu)\alpha_{ns}w_{nsk}\big]e^{\alpha_{ns}z}J_n(\gamma_k r) \tag{13a}$$

$$\sigma_{rzns}=\sum_k^N\mu(\alpha_{ns}u_{nsk}+\gamma_k w_{nsk})e^{\alpha_{ns}z}J_n'(\gamma_k r) \tag{13b}$$

$$\sigma_{\theta zns}=\sum_k^N\mu(\alpha_{ns}\upsilon_{nsk}-nw_{nsk}/r)e^{\alpha_{ns}z}J_n(\gamma_k r) \tag{13c}$$

Because of the $(1/r)$ and $(1/r^2)$ dependences in (13a) and (13c), these expressions are not purely a sum of terms each proportional to $J_n(\gamma_k r)$. To bring them into this form, the following approximations are used

$$\bar{\sigma}_{zzns}\approx\sum_k\sum_q\Big[u_{nsk}\zeta_{kq}^u+\upsilon_{nsk}\zeta_{kq}^\upsilon+w_{nsk}\zeta_{kq}^w\Big]e^{\alpha_{ns}z}J_n(\gamma_k r)$$
$$\bar{\sigma}_{\theta zns}\approx\sum_k\sum_q\Big[\upsilon_{nsk}\xi_{kq}^\upsilon+w_{nsk}\xi_{kq}^w\Big]e^{\alpha_{ns}z}J_n(\gamma_k r) \tag{14a}$$

with the requirement

$$\int_0^a\begin{pmatrix}\bar{\sigma}_{zznk}\\ \bar{\sigma}_{\theta znk}\end{pmatrix}J_n(\gamma_k r)r\,dr=\int_0^a\begin{pmatrix}\sigma_{zznk}\\ \sigma_{\theta znk}\end{pmatrix}J_n(\gamma_k r)r\,dr \tag{14b}$$

Substituting (13a) and (13c) and (14a) in (14b) yield relations for $\zeta_{kq}^{u,\upsilon,w}$ and $\xi_{kq}^{\upsilon,w}$

$$\zeta_{kq}^u=-\lambda\Big(\gamma_k^2\delta_{kq}-n^2h_{kq}^T\Big)/\gamma_k,\quad \zeta_{kq}^\upsilon=\lambda ng_{kq}^T,\quad \zeta_{kq}^w=(\lambda+2\mu)\alpha_s\delta_{kq}$$
$$\xi_{kq}^\upsilon=\mu\alpha_s\delta_{kq},\quad \xi_{kq}^w=-\mu ng_{kq}^T \tag{15a}$$

In terms of barred variables, displacements and stresses become

$$\bar{u}_{ns}=\sum_k^N\sum_q^N C_{nsk}u_{nsk}a_{kq0}e^{\alpha_{ns}z},\quad \bar{v}_{ns}=\sum_k^N\sum_q^N C_{nsk}v_{nsk}c_{kq0}e^{\alpha_{ns}z}$$
$$\bar{w}_{nk}=\sum_k^N\sum_q^N C_{nsk}w_{nsk}c_{kq0}e^{\alpha_{ns}z} \tag{16a}$$

$$\begin{aligned}\bar{\sigma}_{zzns}&=\sum_k^N\sum_q^N C_{nsk}\left[-\lambda(\gamma_k^2c_{kpq0}-n^2c_{kq2})u_{nsk}/\gamma_k+\lambda nc_{kq1}v_{nsk}\right.\\&\left.+(\lambda+2\mu)\alpha_{ns}c_{kq0}w_{nsk}\right]e^{\alpha_{ns}z}\\\bar{\sigma}_{rzns}&=\sum_s^N\sum_q^N C_{nsk}\mu(\alpha_{ns}u_{nsk}+\gamma_kw_{nsk})a_{kq0}e^{\alpha_{ns}z}\\\bar{\sigma}_{\theta zns}&=\sum_k^N\sum_q^N C_{nsk}\mu(\alpha_{ns}c_{kq0}v_{nsk}-nc_{kq1}w_{nsk})e^{\alpha_{ns}z}\end{aligned} \tag{16b}$$

$$\begin{aligned}\bar{\sigma}_{rrns}&=\sum_k^N\sum_q^N C_{nsk}\left[\left((\lambda+2\mu)(-\gamma_k^2c_{kq0}+n^2c_{kq2})/\gamma_k-2\mu b_{kq1}\right)u_{nsk}\right.\\&\left.+\lambda nc_{kq1}v_{nsk}+\lambda\alpha_{ns}c_{kq0}w_{nsk}\right]e^{\alpha_{ns}z}\\\bar{\sigma}_{\theta\theta ns}&=\sum_k^N\sum_q^N C_{nsk}\left[\left(\lambda(-\gamma_k^2c_{kq0}+n^2c_{kq2})/\gamma_k+2\mu b_{kq1}\right)u_{nsk}\right.\\&\left.+(\lambda+2\mu)nc_{kq1}v_{nsk}+\lambda\alpha_{ns}c_{kq0}w_{nsk}\right]e^{\alpha_{ns}z}\\\bar{\sigma}_{r\theta ns}&=\sum_k^N\sum_q^N C_{nsk}\mu(na_{kq1}u_{nsk}+a_{kq0}\gamma_kv_{nsk})e^{\alpha_{ns}z}\end{aligned} \tag{16c}$$

Barred variables in (16) and in what follows are in the transformed space. To return to physical space, consider a vector $\bar{\mathbf{V}}_1$ resulting from the transform

$$\bar{\mathbf{V}}_1=\int_0^a\mathbf{V}_1(r)J_n(\gamma_kr)r\,dr \tag{17a}$$

There exists a vector $\boldsymbol{\beta}_1$ satisfying the expression

$$\begin{aligned}&\mathbf{V}_1(r)=\mathbf{J}_n(r)\boldsymbol{\beta}_1,\\&\boldsymbol{\beta}_1=\{\beta_{1k},\ k=1,N\},\quad \mathbf{J}_n(r)=diag[J_n(\gamma_kr),\ k=1,N]\end{aligned} \tag{17b}$$

Applying the transform to (17b) yields the matrix equation

$$\boldsymbol{\beta}_1=\mathbf{c}_0^{-1}\bar{\mathbf{V}}_1\equiv\bar{\mathbf{c}}_0\bar{\mathbf{V}}_1,\quad \mathbf{c}_0=[c_{kk'0}] \tag{17c}$$

Coefficients $c_{kk'0}$ are defined in (5). Similarly, for

$$\begin{aligned}\bar{\mathbf{V}}_2&=\int_0^a\mathbf{V}_2(r)J_n'(\gamma_kr)r\,dr\Longleftrightarrow\mathbf{V}_2(r)=\boldsymbol{\beta}_2\mathbf{J}_n'(r),\mathbf{J}_n'(r)\\&=diag[J_n'(\gamma_kr),\ k=1,N]\\\boldsymbol{\beta}_2&=\boldsymbol{\alpha}_0^{-1}\bar{\mathbf{V}}_2\equiv\bar{\boldsymbol{\alpha}}_0\bar{\mathbf{V}}_2,\quad \boldsymbol{\alpha}_0=[a_{kk'0}]\end{aligned} \tag{17d}$$

Coefficients $a_{kk'0}$ are also defined in (5).

Let the transformed variables in (16) be combined into a single state vector $\bar{\mathbf{S}}_n$ of length $6N$ including displacements and tractions at an interface: $\bar{\mathbf{S}}_n=\{(\bar{u},\bar{v},\bar{w},\bar{\sigma}_{zz},\bar{\sigma}_{rz},\bar{\sigma}_{\theta z})_{nk},\ k=1,N\}^T$. (16) then becomes

$$\bar{\mathbf{S}}_n(z)=\mathbf{M}_n\mathbf{e}^{\boldsymbol{\alpha}_nz}\mathbf{C}_n\Rightarrow\mathbf{C}_n=\mathbf{M}_n^{-1}\bar{\mathbf{S}}_n(0) \tag{18}$$

where $\mathbf{e}^{\boldsymbol{\alpha}_nz}$ is a diagonal matrix whose s^{th} element is $e^{\alpha_{ns}z}$, $\mathbf{C}_n$ is the vector of modal weights C_{nsk}, and $\mathbf{M}_n$ is the matrix of coefficients in (14a)–(14c). Eq. (18) can be re-written as

$$\bar{\mathbf{S}}_n(z)=\mathbf{M}_n\mathbf{e}^{\boldsymbol{\alpha}_nz}\mathbf{M}_n^{-1}\mathbf{M}_n\mathbf{C}_n=\mathbf{T}_n\bar{\mathbf{S}}_n(0)\Rightarrow\mathbf{T}_n=\mathbf{M}_n\mathbf{e}^{\boldsymbol{\alpha}_nz}\mathbf{M}_n^{-1} \tag{19}$$

Continuity of $\bar{\mathbf{u}}$ and equilibrium of $\bar{\boldsymbol{\sigma}}$ at interfaces of layers is expressed in terms of their respective state vectors $\bar{\mathbf{S}}_{nl}$ where l is layer number. The ensemble of all these conditions at interfaces of layers in addition to boundary conditions at the 2 exterior faces determines a global transfer matrix $\mathbf{T}_G$ in tri-diagonal form operating on the global state vector $\bar{\mathbf{S}}_{Gn}$

$$\mathbf{T}_G\bar{\mathbf{S}}_G=\bar{\mathbf{F}}_o \tag{20a}$$

where $\bar{\mathbf{F}}_o$ is the global vector of external excitation. For a 3-layer stack,

$$\begin{bmatrix}\mathbf{0}&\mathbf{I}&\mathbf{0}&\mathbf{0}&&&&\\\mathbf{t}_{11}^{(1)}&\mathbf{t}_{12}^{(1)}&-\mathbf{I}&\mathbf{0}&&&&\\\mathbf{t}_{21}^{(1)}&\mathbf{t}_{22}^{(1)}&\mathbf{0}&-\mathbf{I}&\mathbf{0}&\mathbf{0}&&\\\mathbf{0}&\mathbf{0}&\mathbf{t}_{11}^{(2)}&\mathbf{t}_{12}^{(2)}&-\mathbf{I}&\mathbf{0}&&\\&&\mathbf{t}_{21}^{(2)}&\mathbf{t}_{22}^{(2)}&\mathbf{0}&-\mathbf{I}&\mathbf{0}&\mathbf{0}\\&&\mathbf{0}&\mathbf{0}&\mathbf{t}_{11}^{(3)}&\mathbf{t}_{12}^{(3)}&-\mathbf{I}&\mathbf{0}\\&&&&\mathbf{t}_{21}^{(3)}&\mathbf{t}_{22}^{(3)}&\mathbf{0}&-\mathbf{I}\\&&&&\mathbf{0}&\mathbf{0}&\bar{\mathbf{u}}_{b2}&\bar{\boldsymbol{\sigma}}_{b2}\end{bmatrix}\begin{Bmatrix}\bar{\mathbf{u}}_1\\\bar{\boldsymbol{\sigma}}_1\\\bar{\mathbf{u}}_2\\\bar{\boldsymbol{\sigma}}_2\\\bar{\mathbf{u}}_3\\\bar{\boldsymbol{\sigma}}_3\\\bar{\mathbf{u}}_4\\\bar{\boldsymbol{\sigma}}_4\end{Bmatrix}=\begin{Bmatrix}\bar{\mathbf{f}}_{o1}\\\mathbf{0}\\\mathbf{0}\\\mathbf{0}\\\mathbf{0}\\\mathbf{0}\\\mathbf{0}\\\mathbf{0}\end{Bmatrix} \tag{20b}$$

$\mathbf{t}_{11}^{(l)}$, $\mathbf{t}_{12}^{(l)}$, $\mathbf{t}_{21}^{(l)}$, $\mathbf{t}_{22}^{(l)}$ are transfer sub-matrices of the lth layer, $\bar{\mathbf{u}}_{b2}=\mathbf{I},\bar{\boldsymbol{\sigma}}_{b2}=\mathbf{0}$ when the last face is fixed, $\bar{\mathbf{u}}_{b2}=\mathbf{0},\bar{\boldsymbol{\sigma}}_{b2}=\mathbf{I}$ when that face is traction-free, and $\bar{\mathbf{f}}_{o1}$ is the transformed external traction over the 1st face. Putting $\bar{\mathbf{F}}_o=0$ in (20a) yields an implicit eigenvalue problem with eigen-set

$$\begin{aligned}\{\overline{\boldsymbol{\Phi}},\omega\}_{nm},\quad \overline{\boldsymbol{\Phi}}_{nm}(r,\theta,z)&=\{\bar{\varphi}(r,z)\cos(n\theta),\bar{\eta}(r,z)\\&\times\sin(n\theta),\bar{\zeta}(r,z)\cos(n\theta)\}_{nm}^T\end{aligned} \tag{21}$$

$\overline{\boldsymbol{\Phi}}_{nm}$ is the mth eigenfunction that implicitly includes all the coupled eigenvalues α_s from eigenproblem (10) and γ_k from (11).

Transient response proceeds by expressing $\mathbf{u}$ as a superposition of two solutions (Berry and Naghdi (1956))

$$\mathbf{u}(r,\theta,z;t)=\mathbf{u}_D(r,\theta,z;t)+\mathbf{u}_S(r,\theta,z)f_p(t) \tag{22}$$

$\mathbf{u}_D$ is the dynamic solution expressed in terms of the eigenfunctions (21) satisfying homogeneous boundary conditions on the exterior faces, where

$$\begin{aligned}u(r,\theta,z;t)&=\sum_{m=1}\sum_{n=0}a_{nm}(t)\varphi_{nm}(r,z)\cos(n\theta)\\v(r,\theta,z;t)&=\sum_{m=1}\sum_{n=0}a_{nm}(t)\eta_{nm}(r,z)\sin(n\theta)\\w(r,\theta,z;t)&=\sum_{m=1}\sum_{n=0}a_{nm}(t)\zeta_{nm}(r,z)\cos(n\theta)\end{aligned} \tag{23}$$

and $\mathbf{u}_S$ is the static solution satisfying the inhomogeneous boundary condition at that face when $f_p(0)=1$ as derived in Section 3. As with $\mathbf{u}_D$, $\mathbf{u}_S$ also decouples for each n as

$$\begin{Bmatrix}u_S\\v_S\\w_S\end{Bmatrix}(r,\theta,z)=\sum_{n=0}\begin{Bmatrix}u_{Sn}(r,z)\cos(n\theta)\\v_{Sn}(r,z)\sin(n\theta)\\w_{Sn}(r,z)\cos(n\theta)\end{Bmatrix} \tag{24}$$

Note that in (23), $\{\varphi,\eta,\zeta\}_{nm}$ in (23) are those in (16a) after transforming back to physical space. Substituting (23) and (24) in (22), and the resulting into (4a)–(4c), then eliminating the r dependence by the integral transforms in (5) yields coupled ordinary differential equations in the generalized coordinates $\mathbf{a}_n(t)=\{a_{nm}(t)\}^T$

$$\mathbf{M}_{gn}\left(\ddot{\mathbf{a}}_n(t)+\boldsymbol{\omega}_n^2\mathbf{a}_n(t)\right)=\mathbf{N}_{an}\ddot{f}_{pn}(t) \tag{25a}$$

$$\begin{aligned}M_{gnmi}&=(1+\delta_{n0})\pi\rho\int_0^a(\varphi_{nm}\varphi_{ni}+\eta_{nm}\eta_{ni}+\zeta_{nm}\zeta_{ni})r\,dr\\N_{anm}&=(1+\delta_{n0})\pi\rho\int_0^a(\varphi_{nm}u_{Sn}+\eta_{nm}v_{Sn}+\zeta_{nm}w_{Sn})r\,dr\end{aligned} \tag{25b}$$

$(\dot{\cdot})$ is derivative with respect to time, and δ_{n0} is the Kroneker delta.

Inverting $\mathbf{M}_{gn}$ in (25a) decouples $a_{nm}(t)$

$$\ddot{\mathbf{a}}_n(t)+\omega^2\mathbf{a}_n(t)=\mathbf{M}_{gn}^{-1}\mathbf{N}_{an}\ddot{f}_{pn}(t) \tag{25c}$$

3. Static analysis

With the time dependence eliminated in (1), solution (3) becomes

$$\begin{aligned}u_{Sn}&=\sum_k U_{nk}(z)J_n'(\gamma_k r)\cos(n\theta)\\ \upsilon_{Sn}&=\sum_k V_{nk}(z)J_n(\gamma_k r)\sin(n\theta)\\ w_{Sn}&=\sum_k W_{nk}(z)J_n(\gamma_k r)\cos(n\theta)\end{aligned} \tag{26}$$

where γ_k are identical to those determined by characteristic Eq. (11). Similarly, subscript n is dropped from there on and will be re-instituted at some point in the derivation. Based on the axisymmetric static solution (El-Raheb, 2002), assume a z solution in the form

$$\begin{aligned}U_k(z)&=u_{Sk}(1+\beta_k^u z)e^{\alpha_k z},\quad V_k(z)=\upsilon_{Sk}(1+\beta_k^\upsilon z)e^{\alpha_k z},\quad W_k(z)\\ &=w_{Sk}(1+\beta_k^w z)e^{\alpha_k z}\end{aligned} \tag{27}$$

$\beta_k^u,\ \beta_k^\upsilon,\ \beta_k^w$ are undetermined constants. Derivatives of (27) follow

$$\begin{aligned}D_k'(z)&=d_{Sk}\left(\alpha_k+\beta_k^d(1+\alpha_k z)\right)e^{\alpha_k z},\\ D_k''(z)&=d_{Sk}\left(\alpha_k^2+\alpha_k\beta_k^d(2+\alpha_k z)\right)e^{\alpha_k z}\\ D_k&\equiv U_k,V_k,W_k,d_{Sk}\equiv u_{Sk},\upsilon_{Sk},w_{Sk}\end{aligned} \tag{28}$$

where $(\,)'$ stands for derivative with respect to z. Substitute (27) and (28) in the static version of Eq. (26), then separate each equation into two parts: Part 1 proportional to $e^{\alpha_k z}$ and Part 2 proportional to $ze^{\alpha_k z}$. Part 1 is

$$\begin{aligned}&\sum_k\big[(\lambda+2\mu)\big(-(\gamma_k^2-n^2/r^2)u_{Sk}+n\gamma_k\upsilon_{Sk}/r+\gamma_k(\alpha_k+\beta_k^w)w_{Sk}\big)\\ &-\mu/r\big(n\gamma_k\upsilon_{Sk}+n^2u_{Sk}/r\big)+\mu\big((\alpha_k^2+2\alpha_k\beta_k^u)u_{Sk}\\ &-\gamma_k(\alpha_k+\beta_k^w)w_{Sk}\big)\big]J_n'(\gamma_k r)-\sum_k\big[(\lambda+2\mu)\big(2n^2u_{Sk}/(\gamma_k r^3)+n\upsilon_{Sk}/r^2\big)\\ &+\mu n\upsilon_{Sk}/r^2\big]J_n(\gamma_k r)=0\end{aligned} \tag{29a}$$

$$\begin{aligned}&\sum_k\big[(\lambda+2\mu)n\big((\gamma_k^2-n^2/r^2)u_{Sk}/(\gamma_k r)-n\upsilon_{Sk}/r-(\alpha_k+\beta_k^w)w_{Sk}\big)\\ &+\mu\big(n(\alpha_k+\beta_k^w)w_{Sk}/r+\alpha_k(\alpha_k+2\beta_k^\upsilon)\upsilon_{Sk}\big)-\mu\upsilon_{Sk}/r^2\\ &+\mu(n^2/r^2-\gamma_k^2)(\gamma_k\upsilon_{Sk}+nu_{Sk}/r)/\gamma_k\big]J_n(\gamma_k r)\\ &-\sum_k\mu\big[\gamma_k\upsilon_{Sk}/r+2nu_{Sk}/r^2\big]J_n'(\gamma_k r)=0\end{aligned} \tag{29b}$$

$$\begin{aligned}&\sum_k\big[(\lambda+2\mu)\big(-(\gamma_k^2-n^2/r^2)(\alpha_k+\beta_k^w)u_{Sk}/\gamma_k+n\gamma_k(\alpha_k+\beta_k^w)\upsilon_{Sk}/r\\ &+\alpha_k(\alpha_k+2\beta_k^w)w_{Sk}\big)+\mu(\gamma_k^2-n^2/r^2)/\gamma_k\big((\alpha_k+\beta_k^u)u_{Sk}-\gamma_k w_{Sk}\big)\\ &-\mu/r\big(n^2w_{Sk}/r+n(\alpha_k+\beta_k^\upsilon)\upsilon_{Sk}\big)\big]J_n(\gamma_k r)=0\end{aligned} \tag{29c}$$

Part 2 is

$$\begin{aligned}&\sum_k\big[(\lambda+2\mu)\big(-(\gamma_k^2-n^2/r^2)\beta_k^u u_{Sk}+n\gamma_k\beta_k^\upsilon\upsilon_{Sk}/r+\gamma_k\alpha_k\beta_k^w w_{Sk}\big)\\ &-\mu/r\big(n\gamma_k\beta_k^\upsilon\upsilon_{Sk}+n^2\beta_k^u u_{Sk}/r\big)+\mu\big(\alpha_k^2\beta_k^u u_{Sk}-\gamma_k\alpha_k\beta_k^w w_{Sk}\big)\big]J_n'(\gamma_k r)\\ &-\sum_k\big[(\lambda+2\mu)\big(2n^2\beta_k^u u_{Sk}/(\gamma_k r^3)+n\beta_k^\upsilon\upsilon_{Sk}/r^2\big)\\ &+\mu n\beta_k^\upsilon\upsilon_{Sk}/r^2\big]J_n(\gamma_k r)=0\end{aligned} \tag{30a}$$

$$\begin{aligned}&\sum_k\big[(\lambda+2\mu)n/r\big((\gamma_k^2-n^2/r^2)\beta_k^u u_{Sk}/\gamma_k-n\beta_k^\upsilon\upsilon_{Sk}/r-\alpha_k\beta_k^w w_{Sk}\big)\\ &-\mu\beta_k^\upsilon\upsilon_{Sk}/r^2-\mu\big(-n\alpha_k\beta_k^w w_{Sk}/r-\alpha_k^2\beta_k^\upsilon\upsilon_{Sk}\big)\\ &+\mu(-n^2/r^2+\gamma_k^2)/\gamma_k(\gamma_k\beta_k^\upsilon\upsilon_{Sk}+n\beta_k^u u_{Sk}/r)\big]J_n(\gamma_k r)\\ &-\sum_k\mu\big[\gamma_k\beta_k^\upsilon\upsilon_{Sk}/r+2n\beta_k^u u_{Sk}/r^2\big]J_n'(\gamma_k r)=0\end{aligned} \tag{30b}$$

$$\begin{aligned}&\sum_k\big[(\lambda+2\mu)\big(-(\gamma_k^2-n^2/r^2)\alpha_k\beta_k^u u_{Sk}/\gamma_k+n\alpha_k\beta_k^\upsilon\upsilon_{Sk}/r+\alpha_k^2\beta_k^w w_{Sk}\big)\\ &-\mu(n^2/r^2-\gamma_k^2)(\alpha_k\beta_k^u u_{Sk}-\gamma_k\beta_k^w w_{Sk})/\gamma_k\\ &-\mu/r\big(n^2\beta_k^w w_{Sk}/r+n\alpha_k\beta_k^\upsilon\upsilon_{Sk}\big)\big]J_n(\gamma_k r)=0\end{aligned} \tag{30c}$$

Multiply (29a) and (30a) by $rJ_n'(\gamma_k r)$, (29b), (29c) and (30b), (30c) by $rJ_n(\gamma_k r)$, and integrate from 0 to a, then divide the integrated (29a) and (30a) by μa_{kk}, and the integrated (29b), (29c) and (30b), (30c) by $(\lambda+2\mu)c_{kk}$ yields

$$\begin{aligned}&[\mathbf{A}_x\ \ \mathbf{A}_y]\begin{Bmatrix}\mathbf{x}\\ \mathbf{y}\end{Bmatrix}+\alpha[\mathbf{B}_x\ \ \mathbf{B}_y]\begin{Bmatrix}\mathbf{x}\\ \mathbf{y}\end{Bmatrix}+\alpha^2\mathbf{x}=\mathbf{0},\quad \mathbf{A}_x\mathbf{y}+\alpha\mathbf{B}_x\mathbf{y}+\alpha^2\mathbf{y}=\mathbf{0}\\ &\mathbf{x}=\{u_S,\upsilon_S,w_S\}_k^T,\quad \mathbf{y}=\{\beta^u u_S,\beta^\upsilon\upsilon_S,\beta^w w_S\}_k^T\end{aligned} \tag{31}$$

Since $\mathbf{x}'=\alpha\mathbf{x}$ and $\mathbf{y}'=\alpha\,\mathbf{y}$, then $\alpha\mathbf{x}'=\alpha^2\mathbf{x}$ and $\alpha\mathbf{y}'=\alpha^2\mathbf{y}$ recasting (32) as

$$\mathbf{x}'-\alpha\mathbf{x}=\mathbf{0}$$

$$[\mathbf{A}_x\quad\mathbf{A}_y]\begin{Bmatrix}\mathbf{x}\\ \mathbf{y}\end{Bmatrix}+[\mathbf{B}_x\quad\mathbf{B}_y]\begin{Bmatrix}\mathbf{x}'\\ \mathbf{y}'\end{Bmatrix}+\alpha\mathbf{x}'=\mathbf{0} \tag{32a}$$

$$\mathbf{y}'-\alpha\mathbf{y}=\mathbf{0}$$

$$\mathbf{A}_x\mathbf{y}+(\mathbf{B}_x+\alpha)\mathbf{y}'=\mathbf{0}$$

$$\Rightarrow\left[\begin{bmatrix}\mathbf{0}&\mathbf{I}&\mathbf{0}&\mathbf{0}\\ -\mathbf{A}_x&-\mathbf{B}_x&-\mathbf{A}_y&-\mathbf{B}_y\\ \mathbf{0}&\mathbf{0}&\mathbf{0}&\mathbf{I}\\ \mathbf{0}&\mathbf{0}&-\mathbf{A}_x&-\mathbf{B}_x\end{bmatrix}-\alpha\begin{bmatrix}\mathbf{I}&\mathbf{0}&\mathbf{0}&\mathbf{0}\\ \mathbf{0}&\mathbf{I}&\mathbf{0}&\mathbf{0}\\ \mathbf{0}&\mathbf{0}&\mathbf{I}&\mathbf{0}\\ \mathbf{0}&\mathbf{0}&\mathbf{0}&\mathbf{I}\end{bmatrix}\right]\begin{Bmatrix}\mathbf{x}\\ \mathbf{x}'\\ \mathbf{y}\\ \mathbf{y}'\end{Bmatrix}=\mathbf{0} \tag{32b}$$

Expressions for the coefficients of $\mathbf{A}_x$, $\mathbf{A}_y$, $\mathbf{B}_x$, $\mathbf{B}_y$ are listed below

$$\begin{aligned}&A_{x11}=(\lambda+2\mu)(n^2e_{jk}-\gamma_k^2\delta_{kj}-2n^2o_{jk}/\gamma_k)/\mu-n^2e_{jk}\\ &A_{x12}=(\lambda+2\mu)(n\gamma_k d_{jk}-nf_{jk})/\mu-n\gamma_k d_{jk}-nf_{jk}\\ &A_{x21}=((\lambda+2\mu)/\mu-1)(\gamma_k^2g_{jk}-n^2l_{jk})n/\gamma_k-2n\bar{m}_{kj}\\ &A_{x22}=-(\lambda+2\mu)n^2h_{jk}/\mu+(n^2-1)h_{jk}-\gamma_k^2\delta_{jk},\ \ A_{x33}=-\mu\gamma_k^2\delta_{jk}/(\lambda+2\mu)\\ &A_{x13}=A_{x23}=A_{x31}=A_{x32}=0\end{aligned} \tag{33a}$$

$$\begin{aligned}A_{y13}&=B_{x13}=((\lambda+2\mu)/\mu-1)\gamma_k\delta_{jk},A_{y23}=B_{x23}\\ &=-((\lambda+2\mu)/\mu-1)ng_{jk}A_{y31}\\ &=B_{x31}-(\mu/(\lambda+2\mu)-1)(\gamma_k^2\delta_{jk}-n^2h_{jk}),\ \ A_{y32}\\ &=B_{x32}-(\mu/(\lambda+2\mu)-1)ng_{jk}A_{y11}=A_{y12}=A_{y21}=A_{y22}\\ &=A_{y33}=B_{x11}=B_{x12}=B_{x21}=B_{x22}=B_{x33}=0B_{ypq}\\ &=0\text{ except for }B_{y11}=B_{y22}=B_{y33}=2\delta_{jk}\end{aligned} \tag{33b}$$

$d_{jk},e_{jk},f_{jk},\ldots,o_{jk}$ are defined in (7d). Solving the eigenvalue problem (32b) produces each eigenvalue and its corresponding eigenvector with a multiplicity of 4 times. To demonstrate this, introduce the dependent variables

$$\mathbf{X}=\{\mathbf{x},\mathbf{x}'\}^T,\quad \mathbf{Y}=\{\mathbf{y},\mathbf{y}'\}^T \tag{34}$$

This re-casts (32b) as

$$\mathbf{A}_1\mathbf{X}+\mathbf{B}_1\mathbf{Y}-\alpha\mathbf{X}=\mathbf{0}$$
$$\mathbf{A}_1\mathbf{Y}-\alpha\mathbf{Y}=\mathbf{0},\mathbf{A}_1=\begin{bmatrix}\mathbf{0} & \mathbf{I}\\ -\mathbf{A}_x & -\mathbf{B}_x\end{bmatrix},\quad \mathbf{B}_1=\begin{bmatrix}\mathbf{0} & \mathbf{0}\\ -\mathbf{A}_y & -\mathbf{B}_y\end{bmatrix} \tag{35}$$

The form of (35) demonstrates that the 2 eigenvalue-problems are not independent and imposes to each eigenvalue a multiplicity of 2. Let the eigenvector be $\mathbf{Y}_m$, i.e. $\mathbf{A}_1\mathbf{Y}_m-\alpha_m\mathbf{Y}_m=\mathbf{0}$. Then from the first in (35)

$$\mathbf{X}_m^*=-[\mathbf{A}_1-\alpha_m\mathbf{I}]_G^{-1}\mathbf{B}_1\mathbf{Y}_m \tag{36}$$

Inspection reveals that $[\mathbf{A}_1-\alpha_m\mathbf{I}]_G$ is singular, so its inverse is a generalized matrix noted by the subscript G, where rows corresponding to the zero divisors are also set to zero. The superscript $(\,)^*$ signifies that the solution is not unique. In fact, if $\bar\alpha$ is any complex number then $\mathbf{X}_m^*=[\bar\alpha\mathbf{I}-[\mathbf{A}_1-\alpha_m\mathbf{I}]_G^{-1}\mathbf{B}_1]\mathbf{Y}_m$ is also a solution of (35). In fact, all that is required are the vectors $\{\mathbf{x}_m,\mathbf{y}_m\}$. Vector $\mathbf{y}_m$ is the top half of $\mathbf{Y}_m$, and $\mathbf{x}_m$ is found from (32a)

$$\mathbf{x}_m^*=-[\mathbf{A}_x+\alpha(\mathbf{B}_x+\alpha_m\mathbf{I})]_G^{-1}[\mathbf{A}_y+\alpha\mathbf{B}_y]\mathbf{y}_m\Rightarrow\mathbf{x}_m=\bar\alpha\mathbf{y}_m+\mathbf{x}_m^* \tag{37}$$

The first bracketed matrix above is also singular, meaning that its inverse must be generalized also. The generalized inverse is determined by singular value decomposition.

For each eigenvalue α_s, the eigenvector dependence on z is

$$\{U_s(z),V_s(z),W_s(z)\}^T=[\mathbf{x}_s^*+(\bar\alpha_s+z)y_s]e^{\alpha_s z} \tag{38}$$

where each pair $\mathbf{x}_s^*,\ \mathbf{y}_s$ is uniquely determined

$$\begin{Bmatrix}x_1^*\\ x_2^*\\ x_3^*\end{Bmatrix}_s(r,\theta)=\sum_{k=1}^{N}\begin{Bmatrix}u_{nsk}J_n'(\gamma_k r)\cos(n\theta)\\ \upsilon_{nsk}J_n(\gamma_k r)\sin(n\theta)\\ w_{nsk}J_n(\gamma_k r)\cos(n\theta)\end{Bmatrix} \tag{39a}$$

$$\begin{Bmatrix}y_1\\ y_2\\ y_3\end{Bmatrix}_s(r,\theta)=\sum_{k=1}^{N}\begin{Bmatrix}u_{nsk}\beta_k^u J_n'(\gamma_k r)\cos(n\theta)\\ \upsilon_{nsk}\beta_k^\upsilon J_n(\gamma_k r)\sin(n\theta)\\ w_{nsk}\beta_k^w J_n(\gamma_k r)\cos(n\theta)\end{Bmatrix} \tag{39b}$$

The complete static solution is expressed through the expansions

$$\begin{aligned}u_S(r,\theta,z)&=\sum_s^{3N}A_s[x_{1s}^*(r,\theta)+(\bar\alpha_s+z)y_{1s}(r,\theta)]e^{\alpha_s z}\\&=\sum_s^{3N}[A_s(x_{1s}^*(r,\theta)+zy_{1s}(r,\theta))+B_s y_{1s}(r,\theta)]e^{\alpha_s z},\\ B_s&=\bar\alpha_s A_s\end{aligned} \tag{40}$$

with similar expansions for υ_S and w_S where subscript 1s is replaced by 2s and 3s respectively. The total number of unknows A_s,B_s totals $6N$. Stress components are also separated in A_s,B_s similar to Eq. (40) using the notation σ_{ijA} and σ_{ijB} for functions factoring A_s and B_s respectively. Also the r, θ, z functions are excluded from the expressions for shortness

$$\begin{aligned}\sigma_{zzA}&=\sum_k[-(\gamma_k^2-n^2/r^2)u_{sk}/\gamma_k+n\upsilon_{sk}/r+w_{sk}(\alpha_s+\beta^w)]\\&\quad+\sum_k z[-(\gamma_k^2-n^2/r^2)\beta^u u_{sk}/\gamma_k+n\beta^\upsilon\upsilon_{sk}/r+\alpha_s\beta^w w_{sk}]\\ \sigma_{rzA}&=\sum_k\mu[\alpha_s u_{sk}(1+z\beta^u)+\beta^u u_{sk}+\gamma_k w_{sk}(1+z\beta^w)]\\ \sigma_{\theta zA}&=\sum_k\mu[\alpha_s\upsilon_{sk}(1+z\beta^\upsilon)+\beta^\upsilon\upsilon_{sk}-nw_{sk}(1+z\beta^w)/r]\end{aligned} \tag{41}$$

As in the dynamic case, σ_{zzA} and $\sigma_{\theta zA}$ must be approximated because of their r dependence. Proceeding along the same steps adopting the factors ζ, ξ defined in Eq. (15a) yields

$$\begin{aligned}\bar\sigma_{zzA}&=\sum_k\sum_q\Big[u_{sk}(1+z\beta^u)\zeta_{kq}^u+\upsilon_{sk}(1+z\beta^\upsilon)\zeta_{kq}^\upsilon\\&\quad+w_{sk}(1+\beta^w/\alpha_s+z\beta^w)\zeta_{kq}^w\Big]J_n(\gamma_k r)\\ \bar\sigma_{\theta zA}&=\sum_k\sum_q\Big[\upsilon_{sk}(1+\beta^\upsilon/\alpha_s+z\beta^\upsilon)\xi_{kq}^\upsilon+w_{sk}(1+z\beta^w)\xi_{kq}^w\Big]J_n(\gamma_k r)\end{aligned} \tag{42}$$

To recover the forms for σ_{zzB}, σ_{rzB} and $\sigma_{\theta zB}$, drop all the $\beta^{u,\upsilon,w}$ terms from σ_{zzA}, σ_{rzA}, $\sigma_{\theta zA}$, and include them in the remaining terms

$$\begin{aligned}\bar\sigma_{zzB}&=\sum_k\sum_q\Big[u_{sk}\beta^u\xi_{kq}^u+\upsilon_{sk}\beta^\upsilon\xi_{kq}^\upsilon+w_{sk}\beta^w\xi_{kq}^w\Big]J_n(\gamma_k r)\\ \bar\sigma_{\theta zB}&=\sum_k\sum_q\Big[\upsilon_{sk}\beta^\upsilon\xi_{kq}^\upsilon+w_{sk}\beta^w\xi_{kq}^w\Big]J_n(\gamma_k r)\end{aligned} \tag{43}$$

To derive the transfer matrix of a layer, combine all the transformed state vectors in a single global vector $\bar{\mathbf{S}}_G^T=\{(u,\upsilon,w,\sigma_{zz},\sigma_{rz},\sigma_{\theta z})_k^s,k=1,\dots,N\}$. Then in terms of the $6N$ unknowns A_s, B_s

$$\bar{\mathbf{S}}_G=[\mathbf{M}+z\widehat{\mathbf{M}}]\mathbf{e}^{\Lambda z}\mathbf{A}+\widehat{\mathbf{M}}\mathbf{e}^{\Lambda z}\mathbf{B} \tag{44}$$

where $\mathbf{e}^{\Lambda z}$ is a diagonal matrix whose sth element is $e^{\alpha_s z}$, $\mathbf{A}$, $\mathbf{B}$ are the vectors of A_s, B_s, $\mathbf{M}$ and $\widehat{\mathbf{M}}$ are each $6N\times 3N$ matrices with an overall layout given in terms of individual 6×1 sub-matrices M_{ks} and $\widehat{M}_{ks}$

$$\begin{aligned}M_{ks1}&=\sum_q u_{sq}a_{qk},\quad M_{ks2}=\sum_q\upsilon_{sq}c_{qk},\quad M_{ks3}=\sum_q w_{sq}c_{qk}\\ M_{ks4}&=\sum_{q'}\sum_q\Big[u_{sq'}\zeta_{q'q}^u+\upsilon_{sq'}\zeta_{q'q}^\upsilon+w_{sq'}(1+\beta^w/\alpha_s)\zeta_{q'q}^w\Big]c_{qk}\\ M_{ks5}&=\sum_q\mu[u_{sq}(\alpha_s+\beta^u)+\gamma_q w_{sq}]a_{qk}\\ M_{ks6}&=\sum_{q'}\sum_q\Big[\upsilon_{sq'}(1+\beta^\upsilon/\alpha_s)\xi_{q'q}^\upsilon+w_{sq'}\xi_{q'q}^w\Big]c_{qk}\\ \widehat{M}_{ks1}&=\sum_q u_{sq}\beta^u a_{qk},\quad \widehat{M}_{ks2}=\sum_q\upsilon_{sq}\beta^\upsilon c_{qk},\quad \widehat{M}_{ks3}=\sum_q w_{sq}\beta^w c_{qk}\\ \widehat{M}_{ks4}&=\sum_{q'}\sum_q\Big[u_{sq'}\beta^u\zeta_{q'q}^u+\upsilon_{sq'}\beta^\upsilon\zeta_{q'q}^\upsilon+w_{sq'}\beta^w\zeta_{q'q}^w\Big]c_{qk}\\ \widehat{M}_{ks5}&=\sum_q\mu[u_{sq}\alpha_s\beta^u+\gamma_q\beta^w w_{sq}]a_{qk},\\ \widehat{M}_{ks6}&=\sum_{q'}\sum_q\Big[\upsilon_{sq'}\beta^\upsilon\xi_{q'q}^\upsilon+w_{sq'}\beta^w\xi_{q'q}^w\Big]c_{qk}\end{aligned} \tag{45}$$

Rewriting (44) as

$$\bar{\mathbf{S}}_G(z)=\begin{bmatrix}\mathbf{M}+z\widehat{\mathbf{M}} & \widehat{\mathbf{M}}\end{bmatrix}\begin{bmatrix}\mathbf{e}^{\Lambda z} & \mathbf{0}\\ \mathbf{0} & \mathbf{e}^{\Lambda z}\end{bmatrix}\begin{bmatrix}\mathbf{A}\\ \mathbf{B}\end{bmatrix} \tag{46a}$$

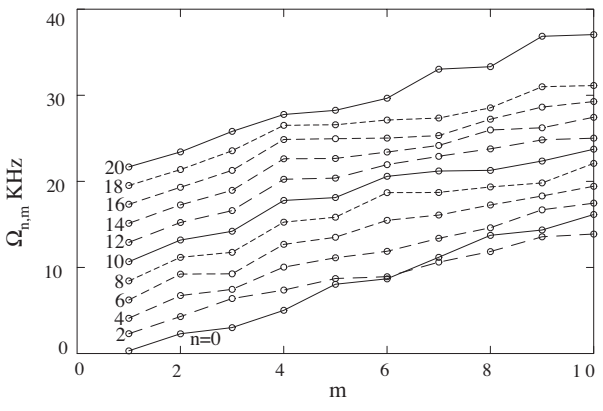

Fig. 2. $\Omega_{n,m}$ spectra of simply supported thick disk.

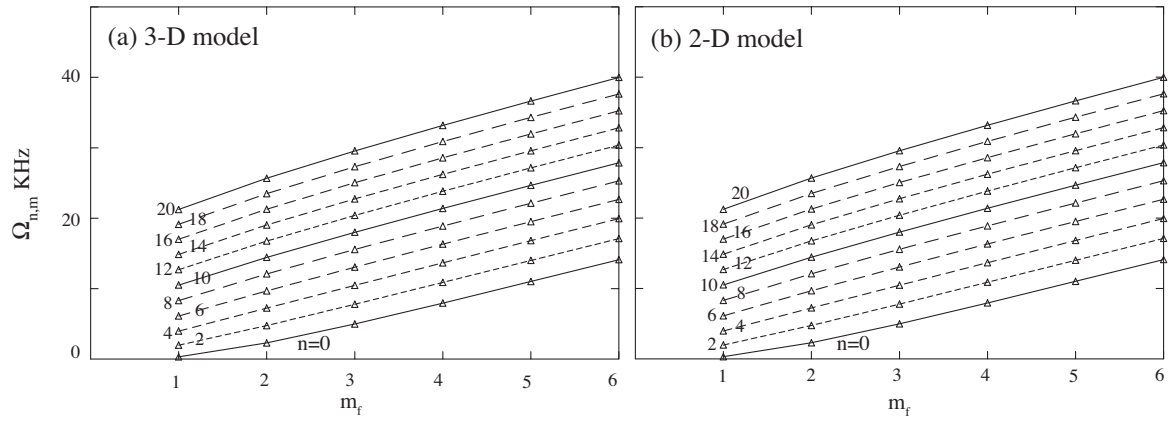

Fig. 3. Flexural resonances of 3-D and 2-D models.

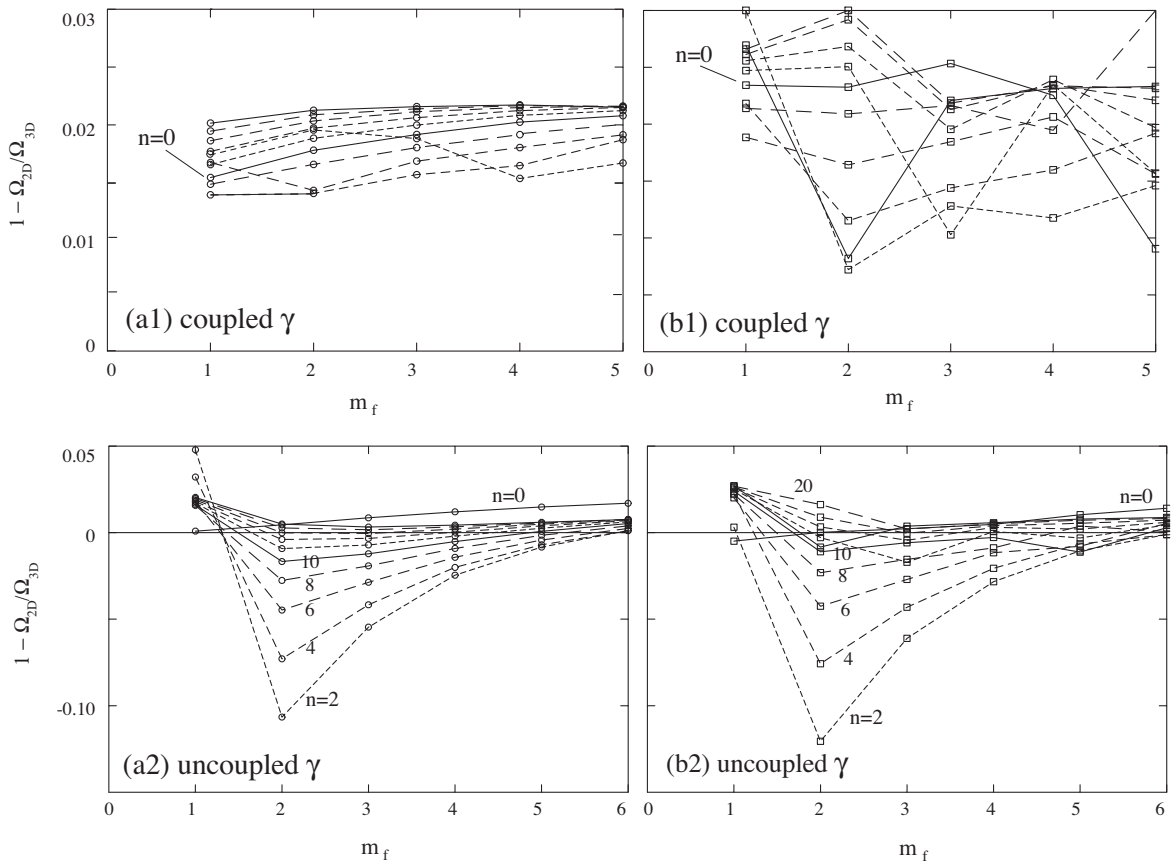

Fig. 4. Difference between 3-D and 2-D flexural resonances 2-D approx. simple supports (a1) coupled γ, (a2) uncoupled γ 2-D exact simple supports (b1) coupled γ, (b2) uncoupled γ.

Evaluating (46a) at $z = 0$ and $z = h$ yields the transfer matrix of a layer

$$\begin{aligned}\bar{\mathbf{S}}_G(0) &= \begin{bmatrix}\mathbf{M} & \widehat{\mathbf{M}}\end{bmatrix}\begin{bmatrix}\mathbf{A}\\ \mathbf{B}\end{bmatrix}\bar{\mathbf{S}}_G(h)\\ &= \begin{bmatrix}\mathbf{M}+h\widehat{\mathbf{M}} & \widehat{\mathbf{M}}\end{bmatrix}\begin{bmatrix}\mathbf{e}^{\Lambda h} & \mathbf{0}\\ \mathbf{0} & \mathbf{e}^{\Lambda h}\end{bmatrix}\begin{bmatrix}\mathbf{A}\\ \mathbf{B}\end{bmatrix}\\ &= \begin{bmatrix}\mathbf{M}+h\widehat{\mathbf{M}} & \widehat{\mathbf{M}}\end{bmatrix}\begin{bmatrix}\mathbf{e}^{\Lambda h} & 0\\ \mathbf{0} & \mathbf{e}^{\Lambda h}\end{bmatrix}\begin{bmatrix}\mathbf{M} & \widehat{\mathbf{M}}\end{bmatrix}^{-1}\\ &= \mathbf{T}(h;0)\bar{\mathbf{S}}_G(0)\end{aligned} \tag{46b}$$

3.1. Results from dynamic analysis

Consider a glass disk with properties

$$E = 90\ \text{GPa},\quad \rho = 2500\ \text{kg/m}^3,\quad \nu = 0.243$$
$$\sigma_u = 100\ \text{MPa},\quad a = 0.6\ \text{m},\quad h = 0.12\ \text{m}$$

σ_u is ultimate strength. The disk is traction free on both faces $z = 0$, h, and satisfies approximate simple supports along the perimeter $r = a$ (see Eq. (11)).

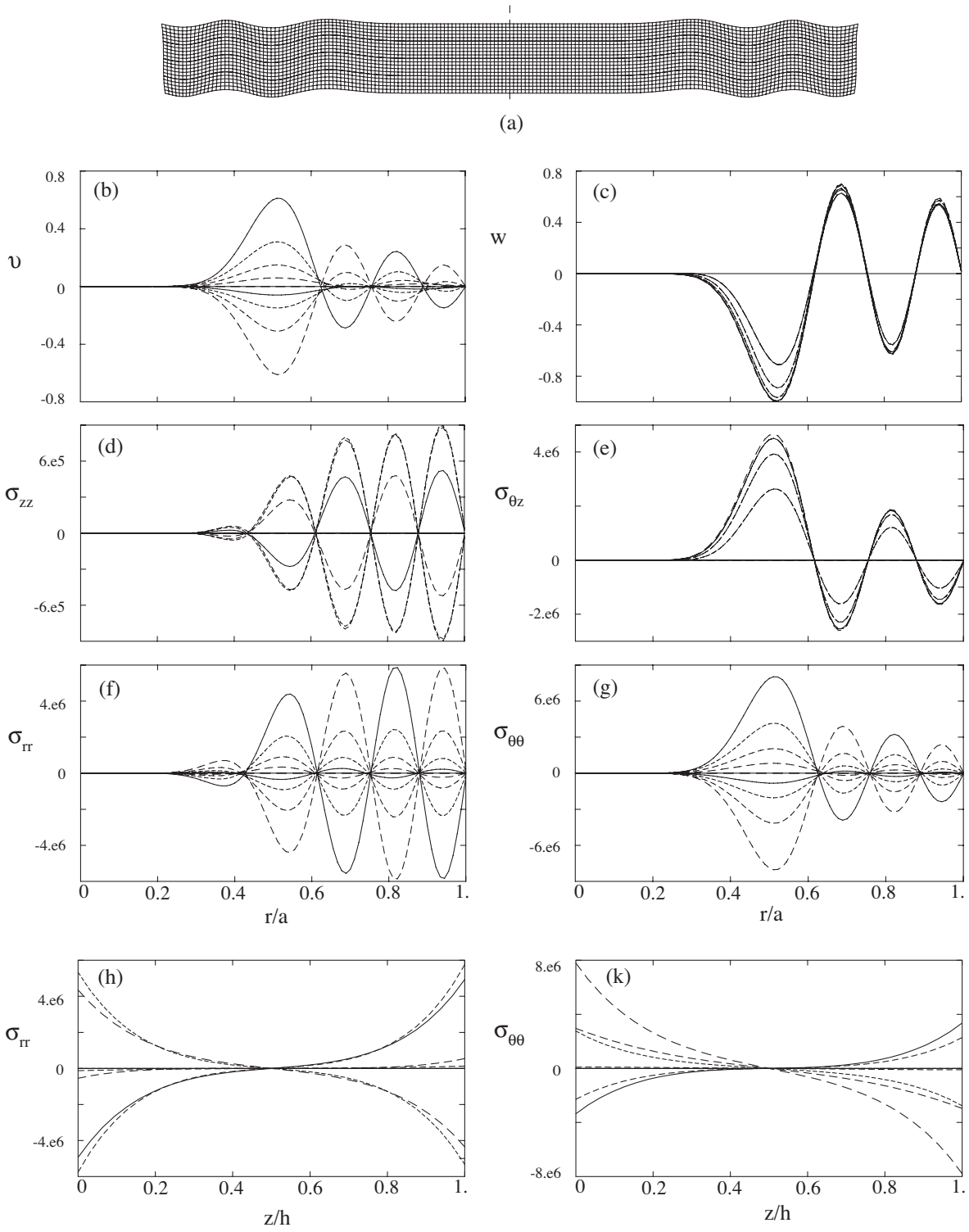

Fig. 5. Modal variables of thick disk for $n = 12$ and $\Omega_{12,7} = 26.27$ kHz (a) flexural mode shape cross-section, (b) $\upsilon(r)$, (c) $w(r)$, (d) $\sigma(r)$, (e) $\sigma_{\theta z}(r)$, (f) $\sigma_{rr}(r)$, (g)$\sigma_{\theta\theta}(r)$; z/h-parameter, (h) $\sigma_{rr}(r)$, (g)$\sigma_{\theta\theta}(z)$; r/a-parameter.

Fig. 2 plots resonant $\Omega_{n,m}$ versus mode number m for $1 \leqslant m \leqslant 10$ with even n as parameter in the range $0 \leqslant n \leqslant 20$. Lines of constant n, termed n-lines, rise uniformly with m. Note that n-lines are not smooth but seem discontinuous, and line $n = 0$ crosses other n-lines. The reason is that the spectrum includes modes of different types: flexural, extensional along r and z, and shear. These types appear intermittently making the ordering of mode number inconsistent with type. In other words, if only flexural modes are plotted versus flexural mode number m_f, then n-lines become smooth and never cross as evidenced by Fig. 3(a). A mode type is identified from its w mode shape.

A comparison of the present 3-D analysis with simpler models like Mindlin's (1951) establishes the limitations of 2-D models and the error committed when using them. In the literature,

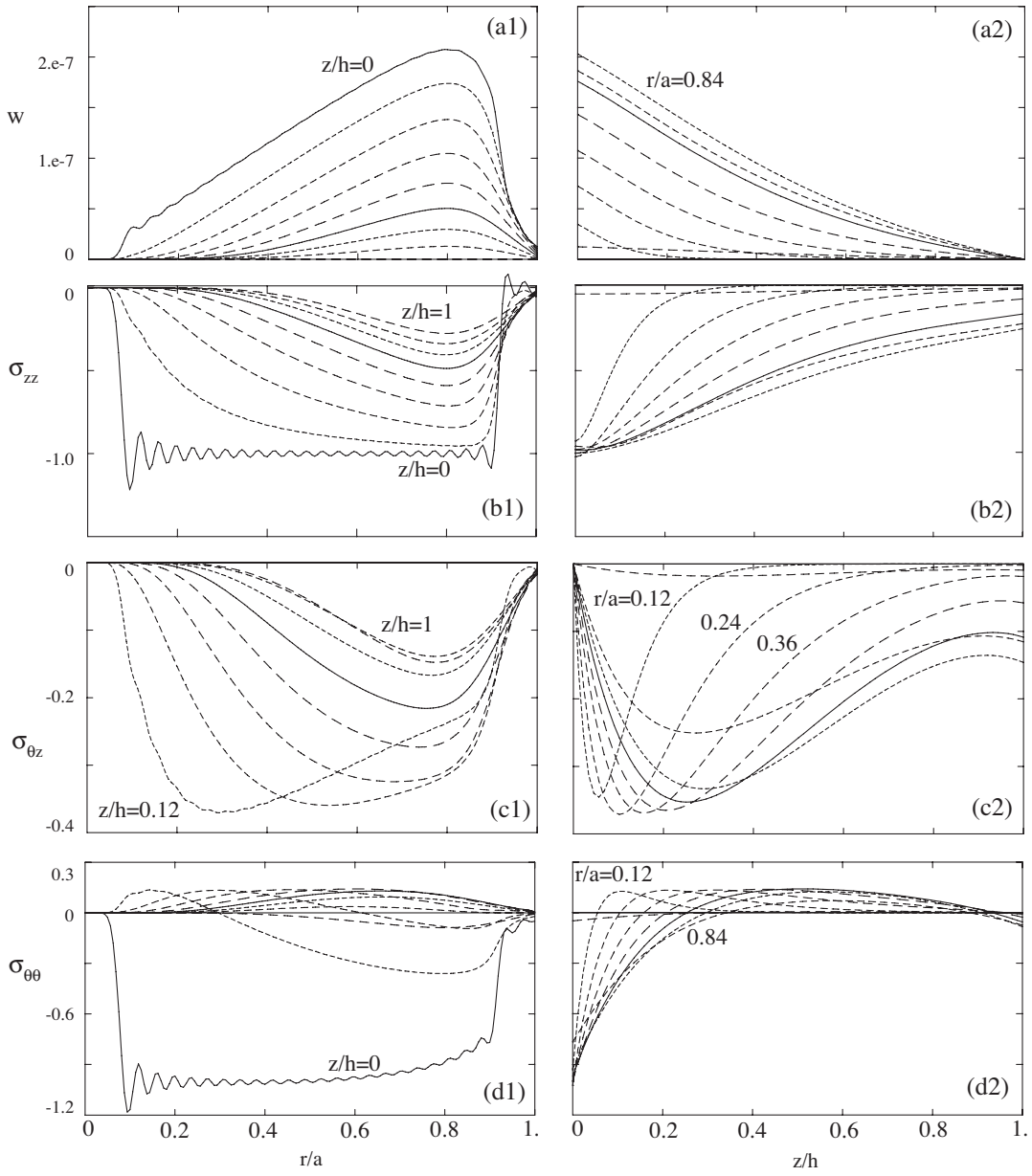

Fig. 6. Static variables from asymmetric pressure with $n = 12$ (a1)–(d1) $w(r)$, $\sigma_{zz}(r)$, $\sigma_{\theta z}(r)$, $\sigma_{\theta\theta}(r)$ with z-parameter (a2)–(d2) $w(z)$, $\sigma_{zz}(z)$, $\sigma_{\theta z}(z)$, $\sigma_{\theta\theta}(z)$ with r-parameter.

comparison of 3-D and 2-D models concerned only axisymmetric motions. An extension to Mindlin's plate equations to include asymmetric motions was formulated and solved analytically by El-Raheb (2002). It is that model that is compared with the present 3-D analysis. In the 2-D model, both approximate boundary condition in Eq. (11) termed SSA, and the exact one termed SSE are used. Fig. 3(b) plots Ω_{2D} versus m_f with n as parameter using SSA. Comparing it with Fig. 3(a) of the 3-D model shows that behavior is the same.

Fig. 4(a1) and (b1) plots the difference $\tilde{d} = (\Omega_{3D} - \Omega_{2D})/\Omega_{3D}$ versus m_f with n as parameter for Ω_{2D} with SSA and SSE respectively. In both cases, $\tilde{d}$ lies between 1 and 2%. To evaluate the effect on resonances of coupling radial wave number γ_k in Eqs. (4) and (6), $\tilde{d}$ is determined for Ω_{3D} with uncoupled γ_k as shown in Fig. 4(a2) and (b2). For these cases, $|\tilde{d}|$ is 3 times grater than $|\tilde{d}|$ in Fig. 4(a1) and (b1) revealing that coupling γ_k improves accuracy of the 3-D solution. This is consistent with results reported by Singh and Subramaniam (2003) for a disk of aspect ratio $h/a = 0.2$, where Ω_{3D} was close to Ω_{2D} adopting a Mindlin model independent of boundary condition.

As an example of an asymmetric resonant mode, consider the flexural mode with four radial half waves $\Omega_{12,7}$ ($n = 12$, $m = 7$) with an r–z cross-section shown in Fig. 5(a). Fig. 5(b)–(g) plot distribution of displacement and stress along r with z/h as parameter at 8 equidistant z stations. Note that all dependent variables become finite for $r/a \geqslant 0.3$, consistent with the property of Bessel function $J_{12}(\gamma_k r)$. Fig. 5(h) and (k) plot σ_{rr} and $\sigma_{\theta\theta}$ along z with r/a as parameter at 6 equidistant r stations. Unlike in 2-D where stress it is proportional to z, in 3-D it varies non-linearly along z.

3.2. Results from static analysis

Consider the same disk as in Section 3.1 but with the bottom face lying on a rigid base and the top face compressed by a hexagon lattice with cyclic segment shown in Fig. A1(b). Along the thickness, the origin of the z-axis is at the center of the loaded face.

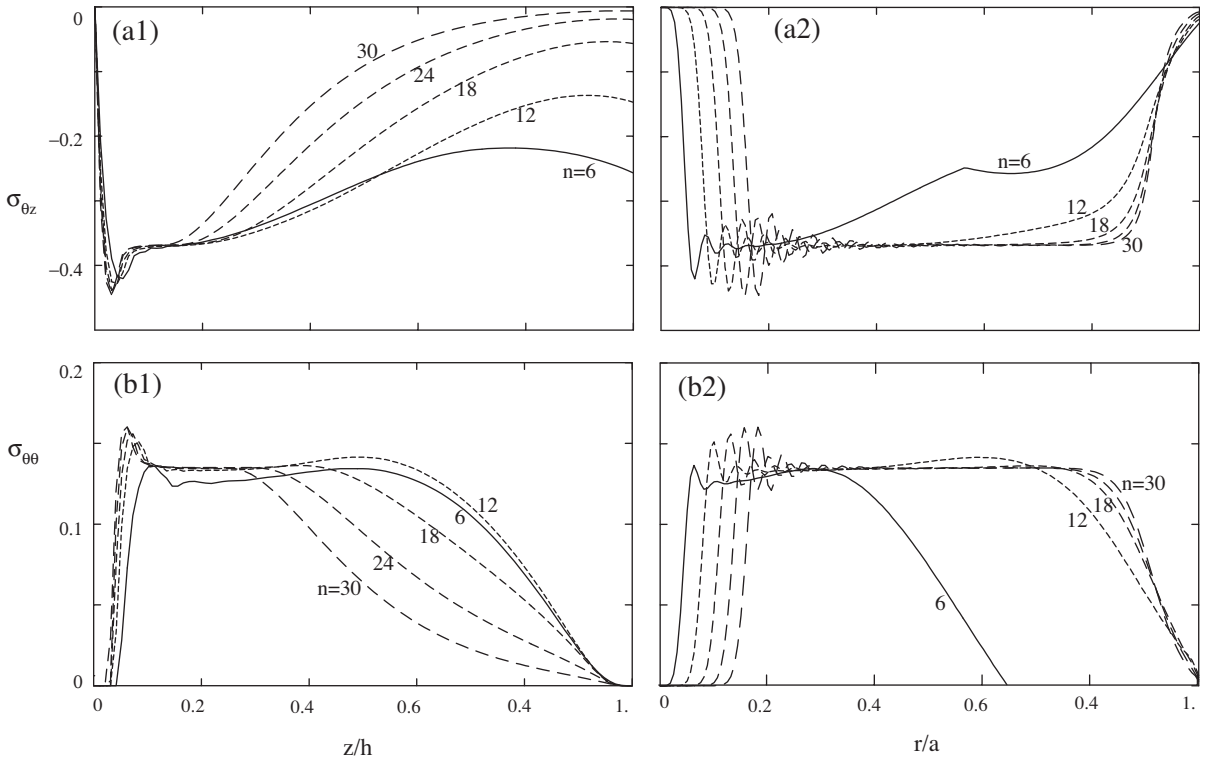

Fig. 7. Maxima and minima along r and z (a1) $|\sigma_{\theta z}|$ max along r versus z, (a2) $|\sigma_{\theta z}|$ max along z versus r (b1) $|\sigma_{\theta\theta}|$ max along r versus z, (b2) $|\sigma_{\theta\theta}|$ max along z versus r.

Assume that pressure applied by the lattice on the disk is uniform under each branch.

Since circumferential dependence $\cos(n\theta)$ is uncoupled, several static solutions each with a different n and with unit pressure are obtained independently. For $n = 12$, Fig. 4 shows distribution of w and 3 stress components along r with z as parameter and along z with r as parameter. Fig. 6(a1) plots w along r. It starts at zero for $r/a \leqslant 0.05$ then rises linearly to a maximum at $r/a = 0.8$ then sharply drops back to zero at $r = a$. Fig. 6(b1) plots σ_{zz} along r. At $z = 0$, σ_{zz} starts from zero at $r/a \leqslant 0.05$ then rises sharply to -1, attaining the prescribed on that face, then continues along that line till it drops to zero at the boundary of the foot-print $r/a = 0.93$. σ_{zz} diminishes uniformly with z because pressure distribution on the forced face varies periodically along θ allowing an expansion across radial node lines that reduces pressure, unlike the axisymmetric case where bulk compression exists throughout the volume. Fig. 6(c1) plots $\sigma_{\theta z}$ along r. At $z = 0$, $\sigma_{\theta z} = 0$ satisfying the boundary condition. At $z/h = 0.12$, $|\sigma_{\theta z}|$ rises sharply reaching a maximum of 0.37 at $r/h = 0.27$. Such large magnitude of shear stress near the forced face and close to the disk center agrees with the location of the observed micro-cracks. This behavior appears also in Fig. 6(c2) as a sharp rise in $|\sigma_{\theta z}|$ along z, and it is repeated at neighboring stations $r/a = 0.24$ and 0.26. Fig. 6(d1) plots $\sigma_{\theta\theta}$ along r. At $z = 0$, $\sigma_{\theta\theta}$ is negative resembling σ_{zz} there. However, at $z/h = 0.12$, $\sigma_{\theta\theta}$ turns positive attaining a maximum of 0.15 then drops back to negative. Again, the small but positive $\sigma_{\theta\theta}$ in the region where $\sigma_{\theta z}$ attains its largest magnitude may lead to a combined principal tensile stress producing the observed superficial micro-cracks.

For other values of n, stress distribution resembles that for $n = 12$ in Fig. 6. A more concise way of presenting results is to plot maximum stress along r versus parameter z/h as in Fig. 6(c1) and (d1), and maximum stress along z versus parameter r/a as in Fig. 6(c2) and (d2). Fig. 7(a1) and (b1) shows that in the vicinity of extrema, distribution of variables from different n solutions follow the same trend. When maxima are plotted versus r/a (see Fig. 7(a2) and (b2)), distribution is comparable to Fig. 7(a1) and (b1) except for a shift in r/a.

The procedure of combining stress from different n solutions to obtain actual stress in the disk starts by expanding in Fourier series the lattice projected line load. This is achieved in Appendix A for the hexagon geometry in Fig. 1(b) with radius 0.56 m. A scaling factor to stress is determined by plotting maximum amplitude F_{mx} from the Fourier series versus number of terms n_{mx} in the expansion. For $0 \leqslant n_{mx} \leqslant 300$, F_{mx} rises smoothly but slowly with n_{mx} approaching a horizontal asymptote, meaning that the series converges. To extend F_{mx} beyond $n_{mx} = 300$ in order to reach the converged value, an accurate non-linear fit is utilized. This determines an approximate factor scaling stress to its asymptotic value from a limited number of static solutions ($n \leqslant 30$)

$$s_F = (F_{as} - F_{mx}(0))/(F_{mx}(30) - F_{mx}(0)) \approx 8.4 \tag{47}$$

F_{as} is the asymptotic F_{mx}. Consequently, data from curves in Fig. 5 can be combined by

$$\sigma_{mx} \approx s_F \sum_{n=6}^{n=30} \overline{C}_{1,n,0}\sigma_{mx}^{(n)} \tag{48}$$

$$\overline{C}_{1,6,0} = 0.02145, \quad \overline{C}_{1,12,0} = 0.02351, \quad \overline{C}_{1,18,0} = 0.03426$$
$$\overline{C}_{1,24,0} = 0.03578, \quad \overline{C}_{1,30,0} = 0.02615$$

where $\overline{C}_{1,n,0}$ is the Fourier coefficient multiplying solution $\sigma_{mx}^{(n)}$ from Fig. 5. This yields combined normalized stresses

$$\sigma_{\theta z} = -0.43, \quad \sigma_{\theta\theta} = 0.16, \quad \sigma_{zz} = -1.0$$
$$\sigma_{rr} = -0.5, \quad \sigma_{rz} = 0.01, \quad \sigma_{r\theta} = 0.01 \tag{49}$$

and principal stresses

$$\sigma_{tens} = 0.31, \quad \sigma_{shr} = 0.72 \tag{50}$$

Since values in (50) are based on unit applied pressure p, then in order not to exceed ultimate stress $\sigma_u = 100$ MPa, p should be limited to

$$p \leqslant \sigma_u \times \sigma_{tens} = 31 \text{ MPa} \quad (\approx 4.5\text{ksi})$$

4. Conclusion

Asymmetric dynamic and static response of a thick disk is analyzed. Noteworthy results follow:

(1) A finite transform in r eliminates it from the governing equations.
(2) In addition to flexural modes, the 3-D model includes extensional and shear dominated modes, and for short wave lengths the difference is not discernable.
(3) Comparing flexural modes from 3-D and 2-D asymmetric models reveals that Ω_{3D} differs by less than 2% from Ω_{2D} independent of boundary condition.
(4) Magnitude of $\sigma_{\theta\theta}$ is greater than all other components by at least 30%.
(5) Unlike 2-D plate theories where flexural stress varies linearly along z, in 3-D it is strongly non-linear.
(6) Coupling radial wave numbers γ_k improves the accuracy of the 3-D model.
(7) For a thick disk statically loaded by a unit pressure varying along θ with wave numbers n, $|\sigma_{\theta z}|$ reaches a maximum in the vicinity of the loaded face. Also, $\sigma_{\theta\theta}$ becomes tensile there.
(8) For a hexagon lattice applying pressure on the disk face, a Fourier decomposition of its projected line-load determines the non-vanishing terms in the series; these are zero and multiples of 6 due to cyclic symmetry of the hexagon.
(9) Also, the Fourier series determine an approximate scaling factor to combined maximum stress from a limited number of static solutions within $6 \leqslant n \leqslant 30$.

Acknowledgment

The Author thanks Dr. James Zwissler of the Jet Propulsion Laboratory for suggesting the problem and for useful discussions on practical issues.

Appendix A. Stress scaling factor from Fourier series

The static load transmitted to the disk is that from a hexagonal lattice with cyclic segment shown in Fig. A1(b). To determine stresses in the disk from this line load requires a 3-D finite element method coupling disk and lattice with a substantial number of elements throughout the volumes of disk and lattice. An approximation expands the lattice projected area in Fourier series. This expansion determines the non-vanishing terms and yields a scale factor to stress from a limited number of static solutions each with different n.

The Fourier series expansion of a hexagon segment is evaluated numerically in a cylindrical coordinate system. Fig. A1(a) shows a rectangular branch, l_f long and h_f wide, in the cyclic segment of the hexagon lattice of Fig. A1(b). Let r be a radial line from the hexagon origin to a point in the rectangle, θ the angle it sustains with the reference X-axis, and ϕ the slope of the rectangle centerline. Let $F(r,\theta) = 1$ be distribution on the lattice to be expanded in Fourier series

$$F(r,\theta) = \sum_{n'=0}^{n_{mx}} \sum_{j=0}^{m_{mx}} \left[\overline{C}_{1n'j} \cos(j\pi r/a_f) + \overline{C}_{2n'j} \sin(j\pi r/a_f) \right] \cos(n'\theta) \tag{A.1}$$

a_f is hexagon radius and equals $n_{ord} l_f$ where n_{ord} is lattice order defined as number of branches on a radial line. Multiplying both sides of (A.1) independently once by $r\cos(n\theta)\cos(m\pi r/a_f)$ and once by $r\cos(n\theta)\sin(m\pi r/a_f)$ then integrating over the domain yields

$$\mathbf{A}\overline{\mathbf{C}} = \mathbf{F}, \quad \mathbf{A} = \begin{bmatrix} \mathbf{A}_{11} & \mathbf{A}_{12} \\ \mathbf{A}_{21} & \mathbf{A}_{22} \end{bmatrix}, \quad \overline{\mathbf{C}} = \begin{Bmatrix} \overline{\mathbf{C}}_1 \\ \overline{\mathbf{C}}_2 \end{Bmatrix}, \quad \mathbf{F} = \begin{Bmatrix} \mathbf{F}_1 \\ \mathbf{F}_2 \end{Bmatrix} \tag{A.2}$$

A_{11} and A_{22} are diagonal matrices with coefficients

$$\begin{aligned} A_{11,nmj} &= \frac{\pi a_f^2}{4} \delta_{mj}(1+\delta_{m0})(1+\delta_{n0}) \\ A_{22,nmj} &= \frac{\pi a_f^2}{4} \delta_{mj}(1-\delta_{m0})(1+\delta_{n0}) \end{aligned} \tag{A.3}$$

where $\delta_{m\,j} = 1$ when $m = j$ and zero otherwise. $\mathbf{A}_{12}$ and $\mathbf{A}_{21}$ are full matrices with coefficients

$$A_{12,nmj} = \begin{cases} -j a_f^2/(j^2-m^2)(1+\delta_{n0}), & m \neq j \\ -a_f^2/(4j)(1+\delta_{n0}), & m = j \end{cases} \tag{A.4}$$

$$A_{21,nmj} = A_{12,njm}(1-\delta_{j0})(1-\delta_{m0})$$

For each rectangular segment in the lattice, the integrals in **F** are

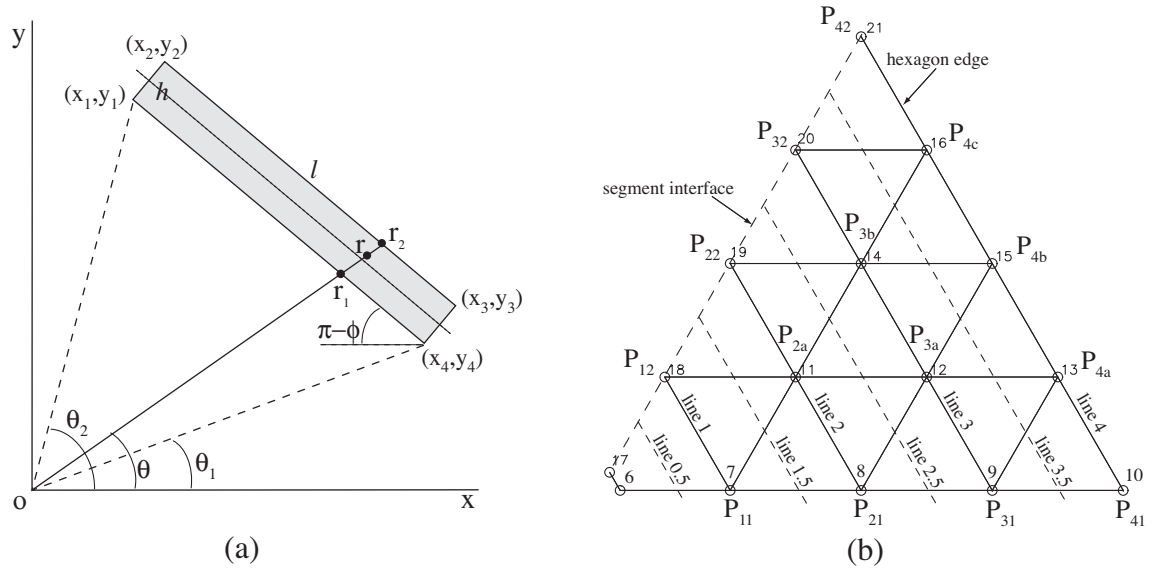

Fig. A1. Branch and cyclic segment of line load from hexagonal frame (a) branch and cylindrical coordinates and (b) cyclic segment.

$$F_{1n,m} = \int_{\theta_1}^{\theta_2} \int_{r_1(\theta)}^{r_2(\theta)} \cos(m\pi r/a_f) r\,dr \cos(n\theta) d\theta$$
$$F_{2n,m} = \int_{\theta_1}^{\theta_2} \int_{r_1(\theta)}^{r_2(\theta)} \sin(m\pi r/a_f) r\,dr \cos(n\theta) d\theta \quad (A.5)$$

$$r_k(\theta) = \left| \frac{(\bar{y}_k - \bar{x}_k \tan\phi)}{\cos\theta(\tan\theta - \tan\phi)} \right|, \quad k = 1,2$$

$(\bar{x}_k, \bar{y}_k)$ are coordinates of intersections of r with sides of the rectangle shown in Fig. A1(a). The integrals in (A.5) are then summed over all branches of the lattice. Since **A** is not diagonal, the series is not orthogonal. For each n, **A** must then be inverted to determine the independent Fourier coefficients $\bar{\mathbf{C}}$

$$\bar{\mathbf{C}} = \mathbf{A}^{-1}\mathbf{F} \quad (A.6)$$

A intermediate result partially validating the analysis is that $F_{1,0,0}$ when summed over all branches of the lattice yields its projected area

$$\sum_{i=1}^{n_b} (F_{1,0,0})_i = S_f = h_f l_f n_b \quad (A.7)$$

where n_b is total number of branches in the lattice. For $h = 0.3$ cm, $l = 14$ cm, and a lattice order $n_{ord} = 4 \Rightarrow n_b = 156$, $S_f = h_f l_f n_b = 0.065$ m^2 that agrees with the sum in (A.7).

Consider the truncated series in (A.1) with $N = 300$ and $M = 100$. Only terms with n being multiples of 6 and zero are finite because of the hexagon cyclic nature. Moreover, only terms with even m are included to insure diagonal $\mathbf{A}_{11}$ and $\mathbf{A}_{22}$.

Fig. A2 plots F versus θ along lines parallel to the outer edges of the hexagon (see Fig. A1(b)). Since $n_{ord} = 4$, there are 4 equidistant parallel branch-lines separated by an interval $\Delta r = l_f \cos(\pi/6)$. Line i is $d_i = i\Delta r$ distant from the center. Also, lines may be located between these branch-lines such as line $(i-1)/2$ distant $d_{(i-1)/2} = (i-1)\Delta r/2$ from the center. These half-lines cross intermediate slant branches as shown in Fig. A1(b). For all lines, sharp peaks appear along radial interfaces of segments at intervals of $\theta = \pi/3$, i.e. P_{i1} and P_{i2} on line i, $i = 1, 4$.

For all lines in Fig. A2, F's lower bound is unity. In a cyclic segment and along lines 2, 3 and 4, Fig. A2(b)–(d) show 1, 2 and 3 additional peaks respectively at branch intersections, i.e. P_{2a} on line 2, $P_{3a,b}$ on line 3, and $P_{4a,b,c}$ on line 4.

Fig. A3 plots F along half-lines 0.5, 1.5, 2.5 and 3.5. As expected, along these lines F has a lower bound of zero because they do not coincide with parallel branches. In a cyclic segment and along lines 1.5, 2.5 and 3.5, Fig. A3(b)–(d) shows 2, 4 and 6 additional peaks respectively at intersections with slant branches, i.e. $P_{1.5a,b}$ on line 1.5, $P_{2.5a,b,c,d}$ on line 2.5, and $P_{3.5a,b,c,d,e,f}$ on line 3.5.

Since observed damage from micro-cracks occurs in the vicinity of disk center where radial dependence is negligible, it is appropriate to set $m = 0$. Fig. A4(a) plots the Fourier coefficients C_{1n0} versus n for $n = 0, 6, 12, \ldots, 300$. After some oscillation with diminishing amplitude, C_{1n0} drops slowly indicating that the series converges. Since the goal of the Fourier analysis is to estimate stress produced by the hexagon lattice pressing on the glass disk, determining 50 static solutions to reach $n = 300$ is impractical. A further approximation is then needed to extrapolate stress from a limited number of n solutions like $n \leqslant 30$. To this purpose, F_{mx} is evaluated as a function of number of terms n_{mx} in the expansion equation (A.1). Fig. A4(b) plots F_{mx} from the Fourier analysis versus n_{mx} for $0 \leqslant n_{mx} \leqslant 300$ where points labeled by open circles.

From Fig. A4(b), it appears that the series has not converged with $n_{mx} = 300$. An accurate extrapolation is then needed to extend the curve to $n_{mx} \gg 300$. For such large n, the procedure employing Eq. (A.2)–(A.6) would lead to erroneous F_{mx} because of inaccuracies in numerical integration. Instead, a non-linear fit based on Marquardt's method is adopted (Marquardt, 1963) for extending F_{mx}. A candidate function to fit that approaches a horizontal asymptote as in Fig. A4(b) is the hyperbolic tangent

$$F_{mx} \approx e_1 + e_2 \tanh(e_3 n + e_4)$$
$$e_1 = -0.772, \quad e_2 = 2.055, \quad e_3 = 0.0185, \quad e_4 = 0.45 \quad (A.8)$$

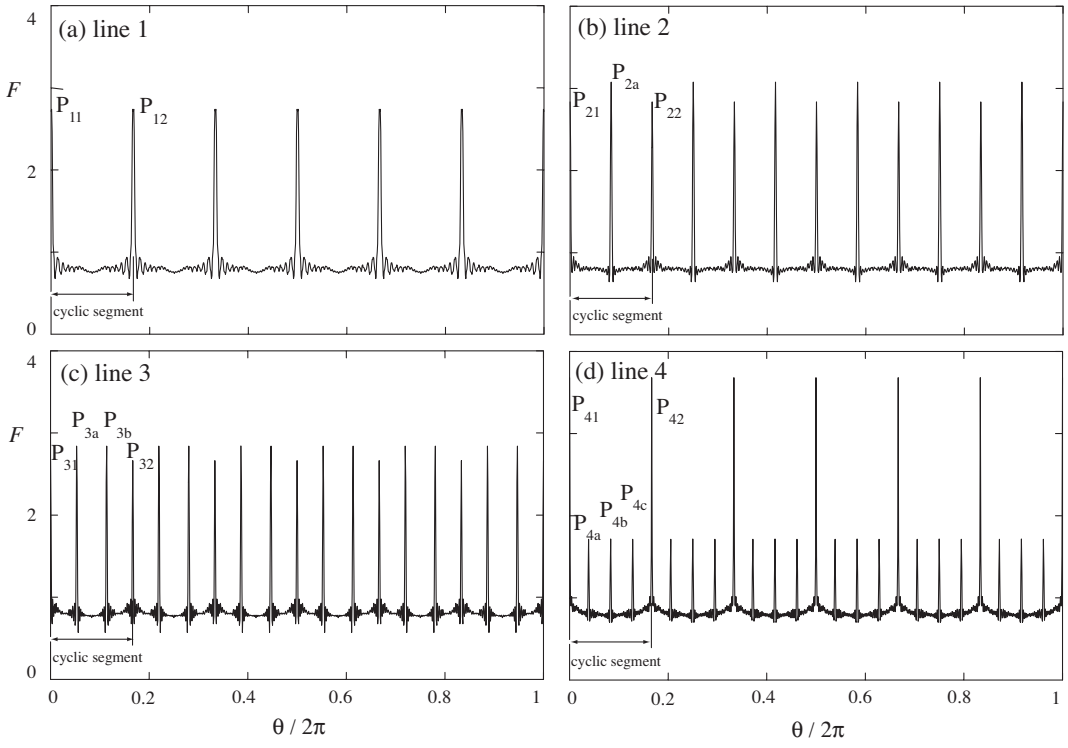

Fig. A2. $F(r,q)$ distribution from Fourier series with $n \geqslant 300$ (a) line 1, (b) line 2, (c) line 3, (d) line 4.

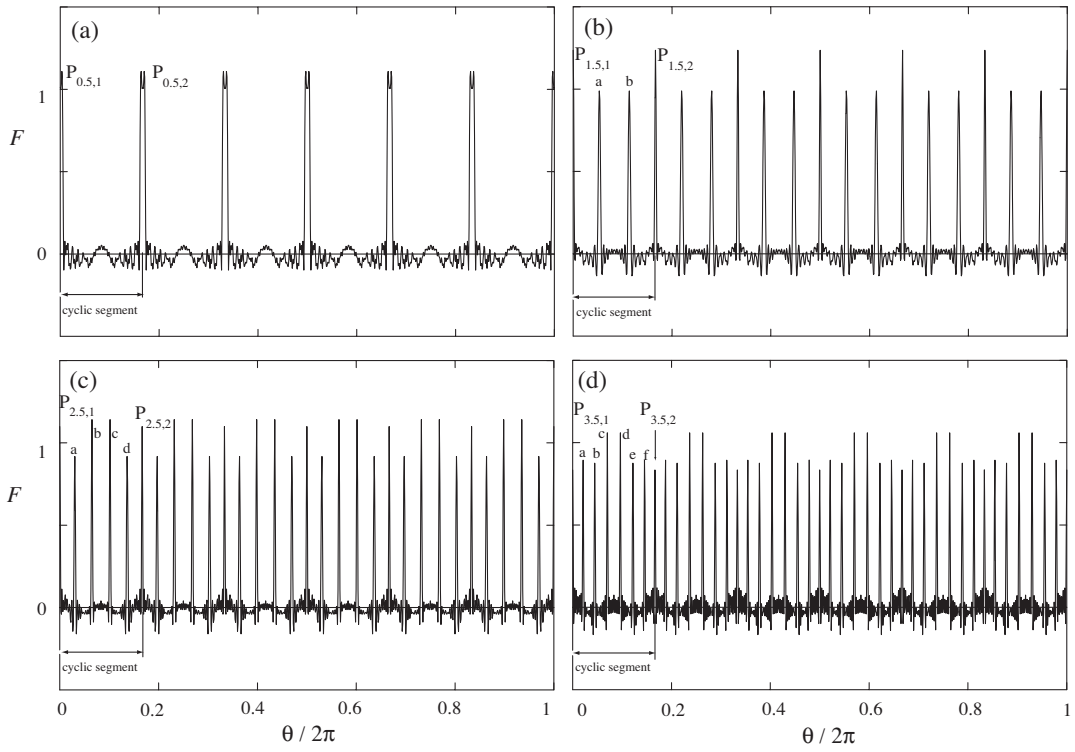

Fig. A3. $F(r,q)$ distribution from Fourier series with $n \geqslant 300$ (a) line 0.5, (b) line 1.5, (c) line 2.5, (d) line 3.5.

The fit depicted by a solid line in Fig. A4(b) matches the values computed from the series in the range $0 \leqslant n \leqslant 300$ with an error not exceeding 0.5%, and extends further with n_{mx} approaching the asymptote.

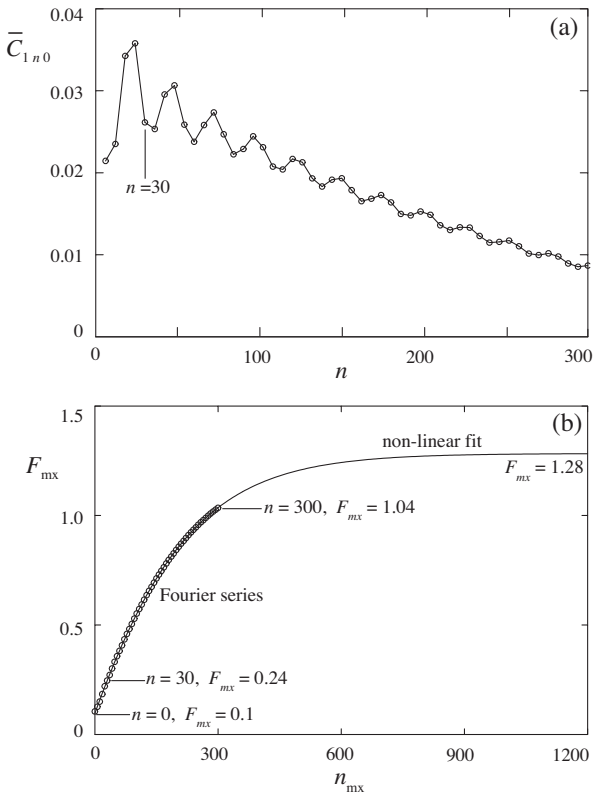

Fig. A4. Fourier series of hexagon lattice (a) Fourier coefficient $\overline{C}_{1n0}$ versus n for $n = 6$, $m = 0$ and (b) F_{mx} versus n_{mx}: ○○○○ Fourier series, — nonlinear fit.

Scaling of $F_{mx}(n_{mx})$ then proceeds as follows. Note from Fig. A4(b) that $F_{mx}(0) = 0.10$, $F_{mx}(30) = 0.24$, $F_{mx}(300) = 1.04$, and $F_{mx}(1200) \approx F_{as} = 1.28$. Since for all n_{mx} the lower bound of F is the same as $F_{mx}(0)$, it implies that $F_{mx}(0)$ depends only on C_{100} independent of n_{mx} and must be subtracted from the $F_{mx}(n_{mx})$ to properly scale $F_{mx}(30)$. Consequently, the approximate scaling factor multiplying solutions $n = 6, 12, \ldots, 30$ is

$$s_F = (F_{as} - F_{mx}(0))/(F_{mx}(30) - F_{mx}(0)) \approx 8.4 \tag{A.9}$$

Given a stress component with a maximum $\sigma_{mx}^{(n)}$ over a range of n, combined stress σ_{mx} for that component is determined by

$$\sigma_{mx} \approx s_F \sum_{n=6}^{n=30} \bar{C}_{1,n,0}\sigma_{mx}^{(n)} \tag{A.10}$$

$$\overline{C}_{1,6,0} = 0.02145, \quad \overline{C}_{1,12,0} = 0.02351, \quad \overline{C}_{1,18,0} = 0.03426$$
$$\overline{C}_{1,24,0} = 0.03578, \quad \overline{C}_{1,30,0} = 0.02615$$

In summary, results from Fourier analysis of the hexagon lattice are

(a) The series is not orthogonal due to the necessary choice of cylindrical coordinates.
(b) Only terms with n equal to zero and multiples of 6 in the series are finite because of cyclic symmetry.
(c) Along lines parallel to the edges, sharp peaks F_{mx} appear along interfaces of cyclic segments and at intersections of branches. F_{mx} is threefold that along intermediate parallel lines.
(d) The lower bound of F depends only on $\bar{C}_{100}$ independent of n_{mx}.
(e) When $m = 0$, F_{mx} rises smoothly but slowly with n_{mx} approaching F_{as} as asymptote.

(f) F_{as} and F_{mx} (30) determine an approximate scaling factor to σ_{mx} from a limited number of static solutions within $6 \leqslant n \leqslant 30$.

References

Berry, J., Naghdi, P., 1956. On the vibration of elastic bodies having time dependent boundary conditions. Quarterly of Applied Mathematics 14, 43–50.

Chen, L., Doong, J., 1984. Vibrations of an initially stressed transversely isotropic circular thick plate. International Journal of Mechanical Sciences 26 (4), 253–263.

Chen, L., Chen, C., 1988. Asymmetric buckling of bi-modulus thick annular plates. Computers & Structures 29 (6), 1063–1074.

Chen, L., Chen, C., 1989. Asymmetric vibration and dynamic stability of bi-modulus thick annular plates. Computers & Structures 31 (6), 1013–1022.

Dong, C., 2008. Three-dimensional free-vibration analysis of functionally graded annular plates using the Chebyshev–Ritz method. Journal of Materials and Design (29), 1518–1525.

El-Raheb, M., Wagner, P., 1996. Transient elastic waves in finite layered media: two-dimensional axisymmetric analysis. Journal of the Acoustical Society of America 99 (6), 3513–3527.

El-Raheb, M., 2002. Dynamic instability of a disk forced by a pulse of short duration. Interantional Journals of Solids and Structure 39 (11), 2965–2986.

Love, A., 1944. A Treatise on the Mathematical Theory of Elasticity, first American edition. Dover Publications Inc., New York, pp. 287–292.

Marquardt, D., 1963. An algorithm for least-squares estimation of non-linear parameters. Journal of the Society of industrial and Applied Mathematics 11 (2), 431–441.

Miklowitz, J., 1984. The theory of elastic waves and wave-guides, first ed. North Holland, Amsterdam, the Netherlands, pp. 214–221.

Mindlin, R., 1951. Influence of rotary inertia and shear deformation on flexural motions of isotropic elastic disks. Transactions of ASME Journal of Applied Mechanics 73, 31–38.

Singh, A., Subramaniam, I., 2003. Vibration of thick circular disks and shells of revolution. Journal of Applied Mechanics. Transactions of ASME 70 (2), 292–298.

Soamidas, V., Ganesan, N., 1991. Vibration analysis of thick, polar orthotropic, variable thickness annular disks. Journal of Sound & Vibration 147 (1), 39–56.

Vinayak, H., Singh, R., 1996. Eigensolutions of annular-like elastic disks with intentionally removed or added material. Journal of Sound & Vibration 192 (4), 741–769.